

Three-dimensional seismic characterization and imaging of the Soda Lake geothermal field

Kai Gao^{*,1}, Lianjie Huang¹, and Trenton Cladouhos²

¹Los Alamos National Laboratory, Geophysics Group, MS D446, Los Alamos, NM 87545, USA

²Cyrq Energy, Inc., 4010 Stone Way North, Suite 400, Seattle, WA 98103, USA

Abstract

Accurate characterization of subsurface geophysical properties and detection of the fault system are essential for geothermal energy exploration and production. The Soda Lake geothermal field is in western Nevada with a complex fault system. Previous seismic characterization only produced a low-resolution, smooth velocity model along with a simple, conceptual fault model. Using optimized correlation-based full-waveform inversion, wavefield-separation-based reverse-time migration, and automatic fault detection techniques, we present 3D seismic characterization for the Soda Lake geothermal field using 3D surface seismic data acquired with Vibroseis sources. We obtain 3D high-resolution velocity, density, and acoustic impedance models, 3D seismic images with different grid spacings, and a high-resolution fault system. Consistency check between the constructed faults and currently active injection and production geothermal wells verifies that our seismic inversion and imaging results and detected faults are reliable. These results can provide valuable information for optimizing well placement and geothermal energy production at the Soda Lake geothermal field.

Keywords: Full-waveform inversion, fault detection, reverse-time migration, Soda Lake geothermal field, surface seismic data

*Corresponding Author: kaigao@lanl.gov (K. Gao); ljh@lanl.gov (L. Huang)

1 Introduction

Geothermal energy is an increasingly important component in the renewable energy sector of the United States. In the continental U.S., western states and Hawaii host most of the geothermal energy resources. The Soda Lake geothermal field is owned and operated by Cyrq Energy, Inc., and is located eight miles north-west of Fallon, Nevada, one of the most geothermal-rich states. Figure 1 shows the location of the Soda Lake geothermal field. The Soda Lake geothermal plant is a binary geothermal electric-generating facility. Soda Lake I operated from 1987 through 2018, and Soda Lake II operated from 1991 through 2019. Figure 1 shows the location of the Soda Lake geothermal field in the U.S. continent and its location in western Nevada.

In this study, we aim to provide a high-resolution, reliable, 3D seismic characterization for the Soda Lake geothermal field using 3D surface seismic data acquired in 2009. Previous studies constructed a low-resolution velocity model for the Soda Lake geothermal field, and built a conceptual fault model based on geophysical imaging and geological analysis. Our goal through this study is to reveal the complexity of subsurface geophysical properties in this region with our recently developed seismic-waveform inversion algorithm, and to construct a high-resolution fault system using our advanced seismic migration imaging and fault construction algorithms in a deterministic and systematic manners.

The 3D surface seismic data acquired at the Soda Lake geothermal field contain a total of 8,321 compressional-to-compressional (PP)-component common-shot gathers. Figure 2 shows the distributions of sources (red dots) and receivers (blue triangles) in this 3D seismic survey. Each common-shot gather covers a surface area of up to approximately $3 \times 3 \text{ km}^2$. The entire survey has a clockwise azimuth angle of 33.97° , measuring from the positive Y direction (i.e., the North direction). There exist some “holes” in the source and receiver distributions where there are no data acquired. The source lines are along the NE-SW direction with a line interval of 235.5 m. The receiver lines are along the NW-SE direction with a line interval of 167.5 m. The inline source interval is 33.5 m, and the inline receiver interval is 67 m. The surface area covered by all the sources and receivers is approximately $6 \times 6 \text{ km}^2$.

To obtain high-resolution subsurface medium parameter models for the Soda Lake geothermal field, we perform full-waveform inversion (FWI) of the acquired 3D surface seismic data. FWI is

a nonlinear inversion method for estimating subsurface medium properties by minimizing the difference between observed seismic waveforms and synthetic waveforms (Tarantola, 1984; Virieux and Operto, 2009). First developed in 1980s, FWI is becoming a standard seismic inversion tool in both theoretical research and industry, particularly for highly complex geology. Suffering from high nonlinearity and the cycle-skipping issue, conventional FWI usually fails to converge to correct results for field seismic data, even for complex synthetic models. We employ our recently developed FWI algorithm that uses a different waveform match criterion in our algorithm to mitigate these difficulties as much as possible, even though not completely. Accompanied with our advanced, parallel full-waveform inversion codes that run on Los Alamos National Laboratory's super-computing platform, we are able to perform a 3D full-waveform inversion for the Soda Lake geothermal field to obtain a set of high-resolution subsurface medium parameter models up to 2.5 km in depth.

A subsurface structural image is one of the most important products from seismic characterization, which provides essential information for geothermal well placement and production. Previous studies have produced a subsurface image using conventional ray-based Kirchhoff migration that is incapable of handling complex structures. To improve subsurface imaging, we apply reverse-time migration to the 3D surface seismic data using our FWI-inverted 3D velocity model. Reverse-time migration (RTM) is an advanced seismic imaging technique for imaging complex structures (McMechan, 1983; Chang and McMechan, 1987). Using the PP seismic data separated from the 3D multi-component seismic data, we perform a wavefield-separation-based low-artifact RTM (Fei et al., 2015) to obtain a high-resolution subsurface structural image for the Soda Lake geothermal field. We subsequently perform a fault-enhancing processing on the 3D RTM image and an automatic fault detection to delineate faults from the 3D image volume.

Through this comprehensive seismic characterization, we achieve a set of high-resolution and reliable 3D subsurface medium parameter models, a 3D structural image, and a 3D fault system for the Soda Lake geothermal field. Our inversion and imaging results reveal a complex fault system unravelling many faults that are not in the previous fault model. We find that current geothermal production wells either penetrate through the faults we detect from the image volume, or are fairly close to these faults. The consistency between the faults and currently active injection/production wells validates the accuracy and reliability of our inversion and imaging results and detected faults.

Our high-resolution 3D subsurface medium property models and 3D fault system image can provide valuable information for optimizing well placement and geothermal energy production at the Soda Lake geothermal field.

Our paper is organized as follows: In the Methodology section, we briefly describe our seismic inversion and imaging methods applied to the 3D surface seismic data from the Soda Lake geothermal field. In the Results section, we present and analyze our seismic inversion and imaging results. Particularly, we perform a check on accuracy and reliability of our imaging and fault detection results by plotting currently active geothermal injection and production wells in the 3D space. We summarize our findings in the Conclusions section.

2 Methodology

The seismic data we use in this study are pre-processed by Geokinetics, an industrial data processing company. Their data processing procedure includes random noise attenuation, groundroll attenuation, surface-consistent deconvolution and amplitude correction, spherical expanding amplitude compensation, and optionally automatic gain control or time-variant spectral whitening, etc. Considering the complexity of 3D seismic data processing for such a large dataset, we perform no additional data processing except frequency-domain filtering and offset-based data selection based on our needs for our 3D seismic inversion and imaging algorithms briefly described in this section.

2.1 Full-waveform inversion

Seismic processing by Geokinetics produced a smooth P-wave velocity model based on migration velocity analysis (MVA) and basalt body building. Figures 3-5 display the smooth P-wave velocity model at three different slicing locations. The MVA also reveals a high-velocity basalt body at the center of the Soda Lake geothermal field, at the depth range of approximately 0.5 to 1 km. All the other regions of the initial velocity model is very smooth and contain almost no any high-wavenumber model perturbations that indicate either faults or sedimentary reflectors.

We employ FWI to derive high-resolution subsurface medium property models for the Soda Lake geothermal field. FWI is a nonlinear inversion approach to estimating medium properties

using both the amplitude and phase information of the full seismic wavefield (Tarantola, 1984; Plessix, 2006; Virieux and Operto, 2009). In its simplest form, FWI is a L_2 -norm nonlinear optimization problem:

$$\psi(\mathbf{m}) = \min_{\mathbf{m}} \frac{1}{2} \|\mathbf{u} - \mathbf{d}\|_2^2, \quad (1)$$

where \mathbf{m} is the model parameter, \mathbf{d} is the observed seismic waveform, and \mathbf{u} is the synthetic seismic waveform. FWI is applicable in either acoustic or elastic media. In our seismic characterization, we use its acoustic form and invert for both the P-wave velocity V_p and the density ρ , i.e., $\mathbf{m} = (V_p, \rho)$. Inverting the density model in addition to the P-wave velocity model facilitates the FWI to achieve better amplitude match. Without including density inversion, some of the reflections caused by acoustic impedance contrasts would be attributed entirely to velocity contrasts of the model, leading to “over-update” of the P-wave velocity model. In this case, visually, the P-wave velocity would contain fairly obvious high-wavenumber perturbations that are geologically less plausible.

FWI in the form of equation (1) is highly nonlinear and difficult to converge because of cycle-skipping issue, particularly for noisy field seismic data. To alleviate these difficulties, we adopt an optimized correlation misfit function in our seismic inversion (Choi and Alkhalifah, 2016):

$$\psi(\mathbf{m}) = \min_{\mathbf{m}} \frac{1}{2} \|\mathcal{C}_\tau(\mathbf{u}, \mathbf{d}) - \mathcal{C}_\tau(\mathbf{d}, \mathbf{d})\|_2^2, \quad (2)$$

where \mathcal{C} is the cross-correlation operation, and τ is the time lag of the cross-correlation. Our studies show that this correlation-based FWI misfit function usually leads to much better convergence and reliable results compared with conventional FWI with equation (1).

In FWI, the inversion gradients associated with the medium parameters are computed using the adjoint-state method (Plessix, 2006; Virieux and Operto, 2009). Our FWI is based on the following first-order form of the acoustic-wave equation:

$$\frac{\partial p}{\partial t} + K \nabla \cdot \mathbf{v} = f, \quad (3)$$

$$\rho \frac{\partial \mathbf{v}}{\partial t} + \nabla p = 0, \quad (4)$$

where $K = \rho V_p^2$ is the bulk modulus of the medium, and f is the source term. We invert for V_p and ρ simultaneously, therefore we compute the gradients associated V_p and ρ based on the wave

equation system as

$$\nabla_{V_p} \psi = - \sum_{N_s, N_r} \int_0^{T_{\max}} \frac{1}{\rho V_p^3} \frac{\partial p}{\partial t} p^\dagger dt, \quad (5)$$

$$\nabla_{\rho} \psi = \sum_{N_s, N_r} \int_0^{T_{\max}} \frac{\partial \mathbf{v}}{\partial t} \mathbf{v}^\dagger dt, \quad (6)$$

where $p = p(\mathbf{x}, t)$ is the source pressure wavefield, p^\dagger is the adjoint-state pressure wavefield, \mathbf{v} and \mathbf{v}^\dagger are the source and adjoint particle velocity wavefields, respectively, N_s and N_r are the numbers of sources and receivers, respectively, and T_{\max} is the maximum propagation time of the wavefield.

The adjoint-state wavefields p^\dagger and \mathbf{v}^\dagger are the solutions to the adjoint-state wave equation with the adjoint source being the external source term, solved in a reverse-time manner. The adjoint source is computed based on equation (2). One can refer [Choi and Alkhalifah \(2016\)](#) for the detailed expression of the adjoint source term.

2.2 Reverse-time migration

High-resolution subsurface structural images can reveal faults that are crucial for optimizing geothermal well placement and production. Conventional imaging such as ray-based Kirchhoff migration can produce satisfactory images for simple structures, but usually fails to provide clear and reliable images when the subsurface geological structures are complex, particularly for faulting geothermal fields.

Reverse-time migration (RTM) is the industrial state-of-the-art imaging technique for imaging complex structures ([McMechan, 1983](#); [Chang and McMechan, 1987](#)). RTM uses full wavefield to form subsurface images. In acoustic media, the PP image is formed by the zero time-lag cross-correlation between the source pressure wavefield and the receiver pressure wavefield. To properly attenuate low-wavenumber artifacts caused by high medium contrasts, as at the Soda Lake geothermal field containing a high-velocity basalt body, we employ the wavefield-separation-based RTM imaging condition ([Fei et al., 2015](#)):

$$I_{pp} = \sum_{N_s, N_r} \int_0^{T_{\max}} [p_s p_r - \mathcal{H}_z(p_s) \mathcal{H}_z(p_r) - p_s \mathcal{H}_z(q_r) - \mathcal{H}_z(p_s) q_r] dt, \quad (7)$$

where N_s and N_r are the numbers of source and receivers, respectively, T_{\max} is maximum wavefield propagation time, and $p_s = p_s(\mathbf{x}, t)$ and $p_r = p_r(\mathbf{x}, t)$ are the source and receiver wavefields,

respectively, with \mathbf{x} being the spatial location and t being the time. The wavefield $q_r = q_r(\mathbf{x}, t) = g(\mathbf{x}) * \mathcal{H}_t(d_0(t))$ is an auxiliary reverse-time-propagated wavefield with the temporal Hilbert transformed seismic data as the source term, $g = g(\mathbf{x})$ is Green's function, and $d_0 = d_0(t)$ is the recorded data at the receiver locations. \mathcal{H}_z denotes the Hilbert transform in the depth direction. The auxiliary dataset $\mathcal{H}_t(d_0(t))$ is computed prior to RTM imaging.

2.3 Fault detection

Directly imaging faults with steep dips is a challenging task using seismic data (e.g., [Tan and Huang, 2014](#)), which requires fault-generated seismic scattering wavefields well preserved in data. For seismic characterization at the Soda Lake geothermal field, we alternatively use post-imaging automatic fault detection method to delineate faults from the 3D seismic image volume produced using the aforementioned RTM algorithm.

We delineate the subsurface fault system at the Soda Lake geothermal field using the optimal fault surface voting method ([Wu and Fomel, 2018](#)). The method first automatically picks a set of sparse seed points from an initial input fault attribute image, and then uses them to construct the optimal surface patch based on global maximum attribute values. The method creates the final fault attribute map, such as the fault likelihood map, from the smoothed attribute maps based on collected accumulation scores. Finally, the method forms fault surfaces based on the computed fault strikes, dips and probabilities. One can refer to [Wu and Fomel \(2018\)](#) for algorithmic details.

We then employ the detected faults to further enhance the RTM PP image with a fault-preserving, nonlinear anisotropic diffusion filtering method ([Fehmers and Höcker, 2003](#); [Wu and Guo, 2018](#)). We process the PP image produced using RTM with the following nonlinear diffusion-type partial differential equation:

$$\frac{\partial I}{\partial t} = \nabla(\varepsilon \mathbf{D} \nabla I), \quad (8)$$

where $I = I(\mathbf{x})$ is the structural image, $\varepsilon = \varepsilon(\mathbf{x})$ is the spatial coherence information, e.g., the detected faults, and $\mathbf{D} = \mathbf{D}(\mathbf{x})$ is the spatially heterogeneous anisotropic diffusion tensor constructed from the structural tensor of the image $I(\mathbf{x})$. Equation (8) can effectively suppress random noises, improve lateral continuity, while enhance faults of the image. One can refer to [Fehmers and Höcker \(2003\)](#) and [Wu and Guo \(2018\)](#) for algorithmic details.

3 Results

3.1 3D full-waveform inversion

The initial MVA P-wave velocity model built by Geokinetics as shown in Figures 3-5 satisfies some kinematic properties of the seismic data. To accommodate our FWI of the 3D surface seismic data from the Soda Lake geothermal field, we resample the initial velocity model with a 10 m regular grid spacing in three spatial directions. This resampling results in a regular-grid initial P-wave velocity model of 603 sample points in both the X- and Y-directions, and 255 sampling points in the depth direction. We build an initial density model using Gardner’s rule (Gardner et al., 1974) as $\rho = 310 \times V_p^{0.25}$ with a unit of kg/m^3 .

Three-dimensional FWI is a computationally intensive inversion problem. Considering that the survey contains over 8,300 common-shot gathers, and the data have a relatively high signal-to-noise ratio after processing, we limit the dominant frequency of inversion to 10 Hz, and we display the inversion results at the 13th iteration.

Figures 6-8 display our FWI-inverted P-wave velocity model at three different slicing locations and view angles. We find apparent layer-structured model perturbations in both the shallow and deep regions compared with the initial smooth velocity model shown in Figures 3-5. Specifically, at the two slicing positions shown in Figures 7 and 8, we observe some faulting discontinuities cutting through the layered structures across the entire model, even at positions that are not beneath the high-contrasted basalt body.

These layer-structured model perturbations and inferred faults are even more clear on our FWI-inverted density model shown in Figures 9-11. For example, in Figure 10, at inline receiver positions spanning from approximately 1.5 km to 5 km, we observe some clear faulting discontinuities that break the layers. Some of these faults are not beneath the basalt body, indicating that they are not artifacts caused by the high medium property contrast of the basalt body. We find similar faulting structures in Figure 11.

The absolute values of the inverted density model might not be accurate out of two possible reasons. First, the seismic data input for the inversion is not truly acoustic, but is PP data separated from the acquired elastic multi-component data. Therefore, their amplitude might not be completely matched with the synthetic acoustic data. Second, we employ a cross-correlation

type misfit function expressed in equation (2). This misfit function facilitates better convergence when using field seismic data, yet does not require a strict absolute amplitude match between the synthetic and the observed waveforms. Nevertheless, this inverted “pseudo-density” model, as described in our Methodology, prevents the inversion producing an over-updated velocity model. In this sense, we consider the inverted density model still has reasonable relative contrasts and accurate structures, although it may not be accurate in terms of absolute values.

With both the FWI-updated P-wave velocity and density models, we compute their corresponding acoustic impedance model shown in Figure 12, where we find clear discontinuities cutting through the layers. These features can be reasonably interpreted as faults in this region. In addition, we find clear layered structures in the acoustic impedance model, which generate reflections in the observed seismic data. These structures are obviously missing in the initial model shown in Figures 3-5. The spatial variations of the inverted models indicate the complexity of the subsurface structures at the Soda Lake geothermal field.

Figure 13 depicts the convergence of the relative data misfit of our FWI over a total of 13 iterations, showing an obvious misfit reduction even with the complexity of both the seismic data and the geological structures in this area. Additional updates may further reduce the data misfit.

In Figure 14, we compare among the observed data (Figure 14a), the synthetic data in the initial model (Figure 14b) and the synthetic data in the FWI-inverted model (Figure 14c), for a randomly selected common-shot gather in the survey. The synthetic data in the initial model are obviously mismatched with the observed data. Particularly, the reflection signals after approximately 1 s in the observed data are completely missing in the synthetic data. By contrast, the match between the synthetic data in the FWI-inverted model and the observed data is clearly improved. Seismic waveforms in Figure 14c before and after 1 s closely resemble those in the observed data in Figure 14a. Other common-shot gathers have also a similar data match improvement after our FWI.

3.2 3D reverse-time migration and fault detection

We subsequently perform 3D reverse-time migration of the 3D surface seismic data from the Soda Lake geothermal field using the FWI-inverted velocity model. The center frequency of the source wavelet used in RTM is also 10 Hz, the same as that used in our FWI.

Figures 15-17 show the structural image up to 2.5 km in depth of the Soda Lake geothermal field at three different slicing positions. We also plot the detected faults along with the images, with colors of the faults representing fault probability. The horizontal slices on the top-left panels of Figures 15-17 show that major faults in this area are along the diagonal direction of the geometry. Interpreted based on the map shown in Figure 1, these major faults are approximately along the north-south direction, with a small to moderate azimuth angle. On the vertical slices, we find the layers in this region are well imaged, even below the high-contrasted basalt body. Faults in this region have steeply dipping angles, as indicated by the fault images in Figures 15-17. Some of these faults penetrate through the basalt body, indicating that the faulting in this region occurred after the basalt body was formed in the geological history.

Figure 18 shows the detected faults from the structural image shown in Figure 15 at three different view angles. Consistent with those shown in Figures 15-17, the colors of the fault surfaces represent the fault probability. Although the fault probability is not full for every spatial point on the fault surfaces, most fault surfaces have moderate to high probability, indicating the detected faults are reliable.

There are several currently active injection and production wells at the Soda Lake geothermal field. To validate the accuracy and reliability of our imaging and fault detection results, we visualize the wells, the structural images, and the detected faults in their true 3D spatial positions, as displayed in Figure 19. Figures 19a and b show several image slices superimposed with the detected faults (in white-blue colors). We place the injection wells (green-colored tubes) and production wells (red-colored tubes) in the 3D space. We find that all the injection and production wells either run through the detected faults or are fairly close to one or two faults. For instance, in Figure 19a, a curved production well in the center of the image penetrates exactly a major fault on the image. The production well on the right of the figure also penetrates a location where two faults intersect. Figure 19b shows that the green-colored injection well on the right of the figure is located adjacent to a major fault, and part of the injection well overlies the fault path.

We show the constructed fault surfaces in Figures 19c-f, along with injection and production wells plotted in the same 3D scene. Clearly, all the production wells either penetrate one or two faults, or are very close to a fault surface. Some of the production wells penetrate through a same fault twice. The consistency between the currently active injection and production wells and our

constructed faults from our 3D image volume demonstrates that our imaging and fault detection results are very close to the realistic geology in this region. The detected fault surfaces consist of a complex fault system in this region.

Our preceding results in this paper reveal complex subsurface structures and medium property variations up to 2.5 km at the Soda Lake geothermal field, with a spatial grid interval of 10 m along lateral and vertical directions. We aim to reveal the complex fault system with a higher spatial resolution using a grid spacing of 6.7 m in the horizontal directions and 2.5 m in the depth direction, up to 1 km in depth for this area. We use a source wavelet with a center frequency of 30 Hz for RTM in this fine grid, enabling us to resolve fine layers for this geothermal field, and to obtain a high-resolution fault system.

Figures 20-22 show the image volume with a horizontal grid spacing of 6.7 m and a vertical grid spacing of 2.5 m, superimposed by the detected faults from this image volume. We observe that the detected faults have similar strikes with those shown in Figures 15-17. These high-resolution images and detected faults further verify the geological complexity of the near-surface region up to 1 km in depth.

We further construct fault surfaces using the high-resolution image volume shown in Figures 20-22. Figure 23 show the constructed fault surfaces at three different view angles. These fault surfaces have relatively higher overall fault probability compared with those associated with the 10-m-grid-spacing image shown in Figure 18. Some of these faults are not properly detected from the 10-m-grid-spacing image. We also find interlacing fault surfaces in Figure 23, which further verify that the fault system at the Soda Lake geothermal field is fairly complex, and requires high-resolution images to reveal those faults.

Similar to the examination on the fault-well consistency for the 10-m-grid-spacing image, we show in Figure 24 that all currently active injection and production wells either run through or are very close to our detected faults. This fault-well consistency, along with that associated with the 10-m-grid-spacing image volume, further verifies the accuracy and reliability of our subsurface fault imaging at the Soda Lake geothermal field.

4 Conclusions

We have conducted a 3D, high-resolution seismic characterization for the Soda Lake geothermal field using full-waveform inversion and reverse-time migration of 3D surface seismic data. We have obtained updated velocity, density, and acoustic impedance models using 3D full-waveform inversion of the pre-processed 3D PP seismic data. We have also performed high-resolution, wavefield-separation-based reverse-time migration to obtain high-resolution 3D structural images, including a 10-m-grid-spacing image up to 2.5 km in depth, and a high-resolution image with a vertical grid spacing of 2.5 m up to 1 km. We have detected faults from these image volumes and constructed corresponding fault surfaces, revealing the complex fault system at the Soda Lake geothermal field. A careful check on the consistency between the constructed fault surfaces and current active injection and production wells validate that our seismic inversion and imaging results and detect faults are accurate and reliable. These results can provide valuable information for optimizing well placement and geothermal energy production. Future work aims at using multi-component elastic seismic data to conduct isotropic and anisotropic elastic full-waveform inversion to reveal anisotropic characteristics of the Soda Lake geothermal field.

5 Acknowledgments

This work was supported by the U.S. Department of Energy (DOE) Geothermal Technologies Office through the Los Alamos National Laboratory (LANL). LANL is operated by Triad National Security, LLC, for the U.S. DOE National Nuclear Security Administration (NNSA) under Contract No. 89233218CNA000001. This research used resources provided by the LANL Institutional Computing Program supported by the U.S. DOE NNSA under Contract No. 89233218CNA000001. We thank Xinming Wu and Benxin Chi for helpful discussions, and David Li for his review of the manuscript.

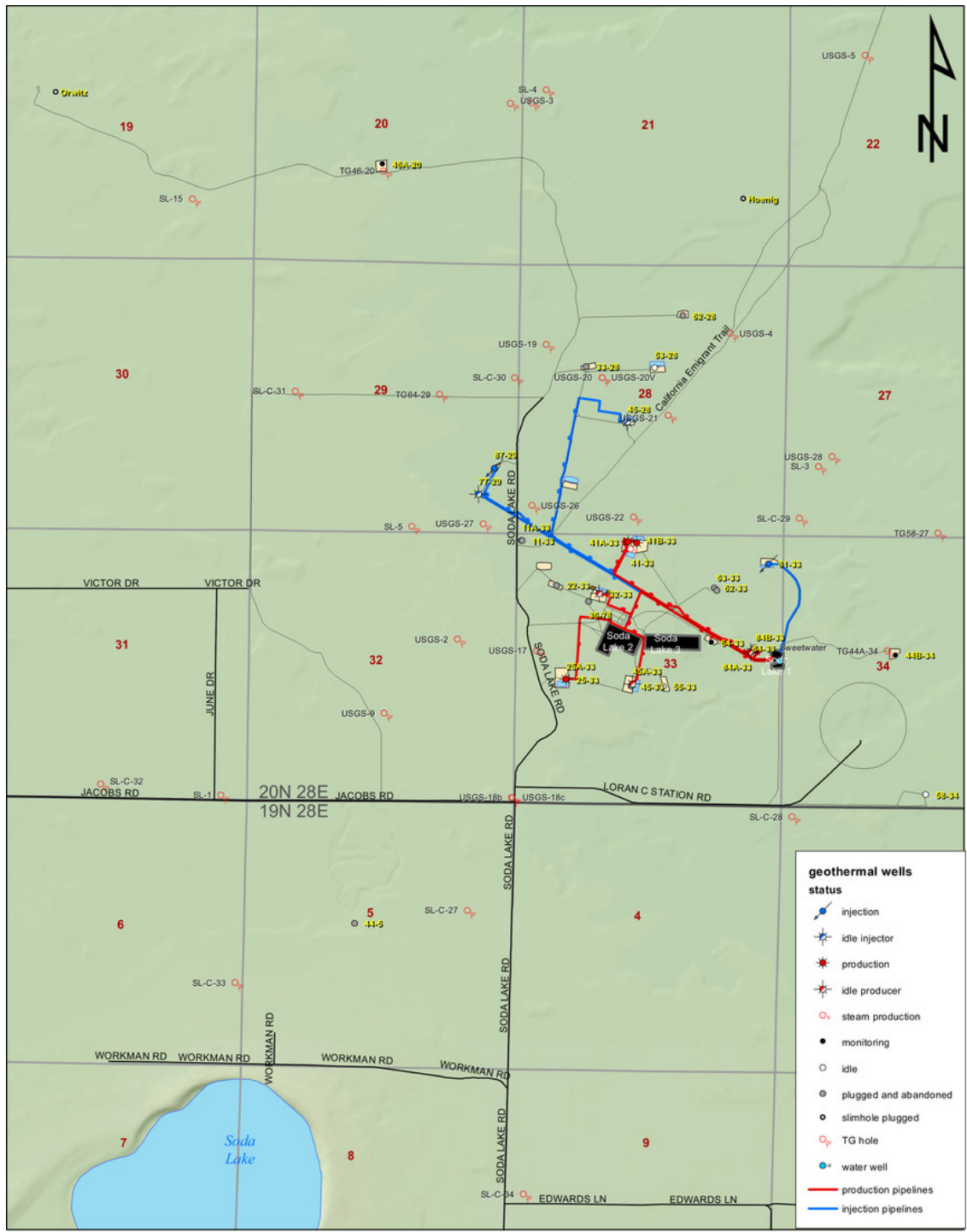
References

- Chang, W.-F., and G. A. McMechan, 1987, Elastic reverse-time migration: *Geophysics*, **52**, no. 10, 1365–1375, doi: 10.1190/1.1442249.
- Choi, Y., and T. Alkhalifah, 2016, An optimized correlation-based full waveform inversion: Conference Proceedings of 78th EAGE Conference and Exhibition, **2016**, no. 1, 1–5, doi: 10.3997/2214-4609.201600642.
- Fehmers, G. C., and C. F. W. Höcker, 2003, Fast structural interpretation with structure-oriented filtering: *Geophysics*, **68**, no. 4, 1286–1293, doi: 10.1190/1.1598121.
- Fei, T. W., Y. Luo, J. Yang, H. Liu, and F. Qin, 2015, Removing false images in reverse time migration: The concept of de-primary: *Geophysics*, **80**, no. 6, S237–S244, doi: 10.1190/geo2015-0289.1.
- Gardner, G. H. F., L. W. Gardner, and A. R. Gregory, 1974, Formation velocity and density: The diagnostic basics for stratigraphic traps: *Geophysics*, **39**, no. 6, 770–780, doi: 10.1190/1.1440465.
- McMechan, G. A., 1983, Migration by extrapolation of time-dependent boundary values: *Geophysical Prospecting*, **31**, no. 3, 413–420, doi: 10.1111/j.1365-2478.1983.tb01060.x.
- Plessix, R.-E., 2006, A review of the adjoint-state method for computing the gradient of a functional with geophysical applications: *Geophysical Journal International*, **167**, no. 2, 495–503, doi: 10.1111/j.1365-246X.2006.02978.x.
- Tan, S., and L. Huang, 2014, Least-squares reverse-time migration with a wavefield-separation imaging condition and updated source wavefields: *Geophysics*, **79**, no. 5, S195–S205, doi: 10.1190/geo2014-0020.1.
- Tarantola, A., 1984, Inversion of seismic reflection data in the acoustic approximation: *Geophysics*, **49**, no. 8, 1259–1266, doi: 10.1190/1.1441754.
- Virieux, J., and S. Operto, 2009, An overview of full-waveform inversion in exploration geophysics: *Geophysics*, **74**, no. 6, WCC1–WCC26, doi: 10.1190/1.3238367.
- Wu, X., and S. Fomel, 2018, Automatic fault interpretation with optimal surface voting: *Geophysics*, **83**, no. 5, O67–O82, doi: 10.1190/geo2018-0115.1.
- Wu, X., and Z. Guo, 2018, Detecting faults and channels while enhancing seismic structural and stratigraphic features: *Interpretation*, **7**, no. 1, T155–T166, doi: 10.1190/INT-2017-0174.1.

List of Figures

| | | |
|----|---|----|
| 1 | Location of the Soda Lake geothermal field in the western Nevada. | 16 |
| 2 | Source and receiver distributions of the 3D surface seismic survey at the Soda Lake geothermal field. The survey contains 8,321 common-shot gathers. Each common-shot gather has a coverage area of up to approximately $3 \times 3 \text{ km}^2$ | 17 |
| 3 | Slices and a 3D view of the initial P-wave velocity model produced by Geokinetics at slicing position 1. | 18 |
| 4 | Slices and a 3D view of the initial P-wave velocity model produced by Geokinetics at slicing position 2. | 19 |
| 5 | Slices and a 3D view of the initial P-wave velocity model produced by Geokinetics at slicing position 3. | 20 |
| 6 | Slices and a 3D view of the updated P-wave velocity model produced using our FWI at slicing position 1 | 21 |
| 7 | Slices and a 3D view of the updated P-wave velocity model produced using our FWI at slicing position 2. | 22 |
| 8 | Slices and a 3D view of the updated P-wave velocity model produced using our FWI at slicing position 3. | 23 |
| 9 | Slices and a 3D view of the updated density model produced using our FWI at slicing position 1. | 24 |
| 10 | Slices and a 3D view of the updated density model produced using our FWI at slicing position 2. | 25 |
| 11 | Slices and a 3D view of the updated density model produced using our FWI at slicing position 3. | 26 |
| 12 | Slices and a 3D view of the updated acoustic impedance model produced using our FWI. | 27 |
| 13 | Data misfit convergence over a total of 13 iterations in our FWI. | 28 |
| 14 | Panels (a)-(c) show the observed data, the synthetic data in the initial model shown in Figure 3, and the synthetic data in the FWI-updated model shown in Figure 6, respectively. | 29 |
| 15 | Slices and a 3D view of the structural image of the Soda Lake geothermal field up to 2.5 km in depth produced with our fault-enhancing RTM algorithm, superimposed with the detected faults at slicing position 1. | 30 |
| 16 | Slices and a 3D view of the structural image of the Soda Lake geothermal field up to 2.5 km in depth produced with our fault-enhancing RTM algorithm, superimposed with the detected faults at slicing position 2. | 31 |
| 17 | Slices and a 3D view of the structural image of the Soda Lake geothermal field up to 2.5 km in depth produced with our fault-enhancing RTM algorithm, superimposed with the detected faults at slicing position 3. | 32 |
| 18 | Panels (a)-(c) show the constructed fault surfaces from the RTM structural image shown in Figure 15 at three different view angles. Colors of the fault surfaces represent the fault probability and are consistent with those in Figures 15-17. | 33 |

| | | |
|----|---|----|
| 19 | Panels (a)-(b) show the detected faults for the RTM structural image shown in Figure 15 at two different view angles, along with active injection (green) and production (red) wells at the Soda Lake geothermal field. Panels (c)-(f) show the constructed fault surfaces with currently active injection and production wells in this geothermal field. | 34 |
| 20 | Slices and a 3D view of the structural image up to 1 km in depth produced with our fault-enhancing RTM algorithm, superimposed by the detected faults at slicing position 1. | 35 |
| 21 | Slices and a 3D view of the structural image up to 1 km in depth produced with our fault-enhancing RTM algorithm, superimposed by the detected faults at slicing position 2. | 36 |
| 22 | Slices and a 3D view of the structural image up to 1 km in depth produced with our fault-enhancing RTM algorithm, superimposed by the detected faults at slicing position 3. | 37 |
| 23 | Panels (a)-(c) show the detected faults from the structural image volume shown in Figure 20 at three different view angles. Colors of the fault surfaces represent fault probability and are consistent with those in Figures 20-22. | 38 |
| 24 | Panels (a)-(b) show the constructed fault surfaces from the structural image shown in Figure 20 at two different view angles, along with active injection (green) and production (red) wells in this area. Panels (c)-(f) depict the constructed fault surfaces with currently active injection and production wells at the Soda Lake geothermal field. | 39 |



MWS - 4/20/20



SLO AMOR IX LLC
Churchill County

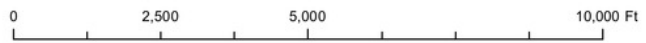


Figure 1: Location of the Soda Lake geothermal field in the western Nevada.

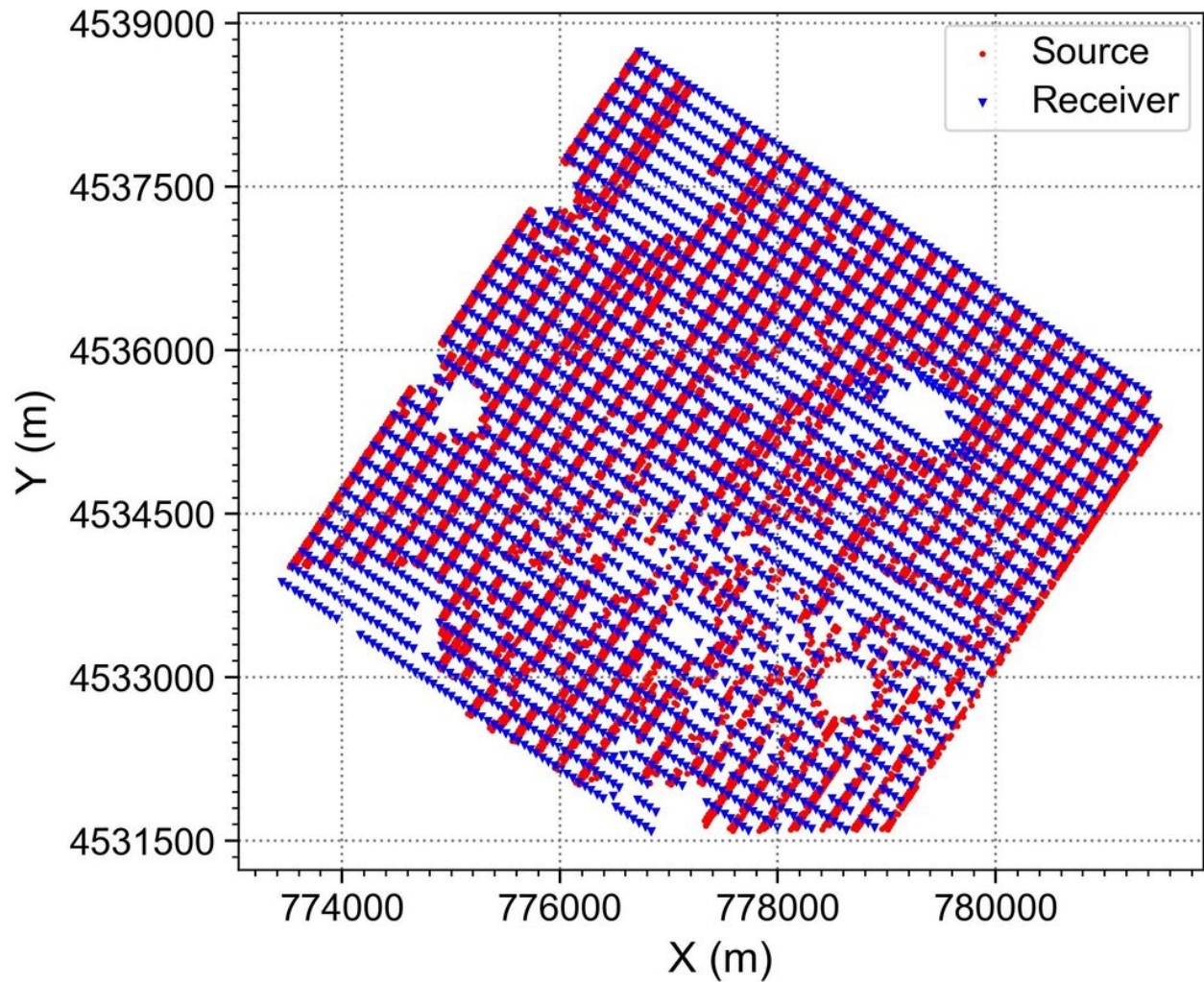


Figure 2: Source and receiver distributions of the 3D surface seismic survey at the Soda Lake geothermal field. The survey contains 8,321 common-shot gathers. Each common-shot gather has a coverage area of up to approximately $3 \times 3 \text{ km}^2$.

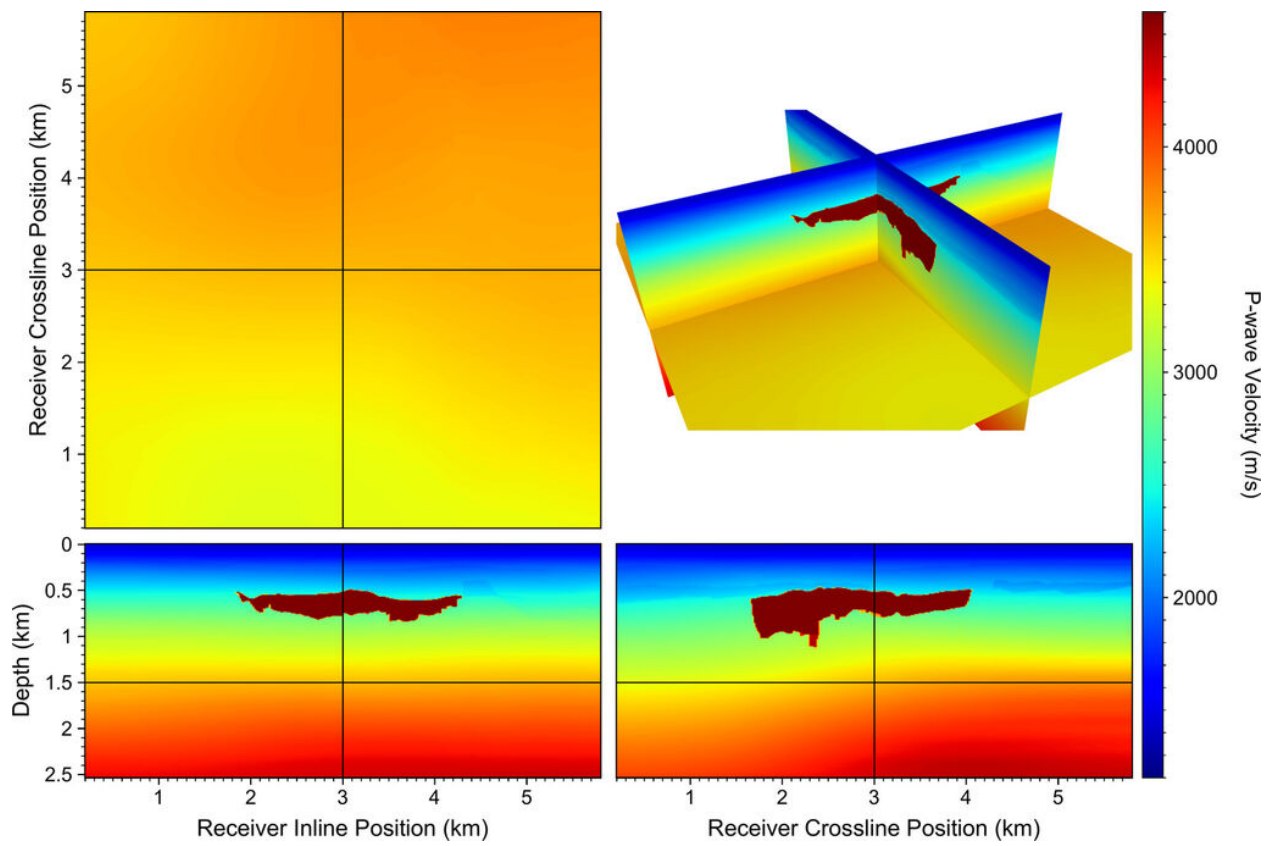


Figure 3: Slices and a 3D view of the initial P-wave velocity model produced by Geokinetics at slicing position 1.

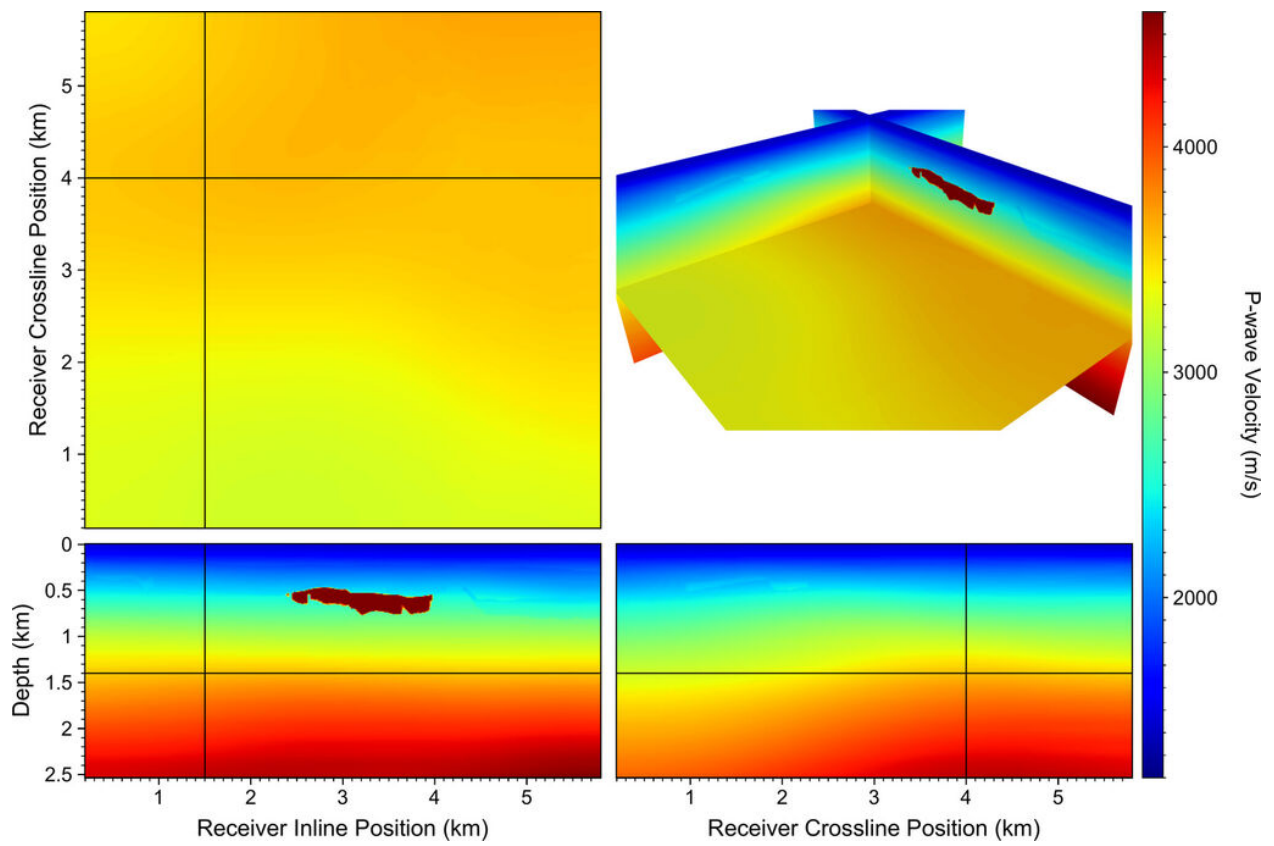


Figure 4: Slices and a 3D view of the initial P-wave velocity model produced by Geokinetics at slicing position 2.

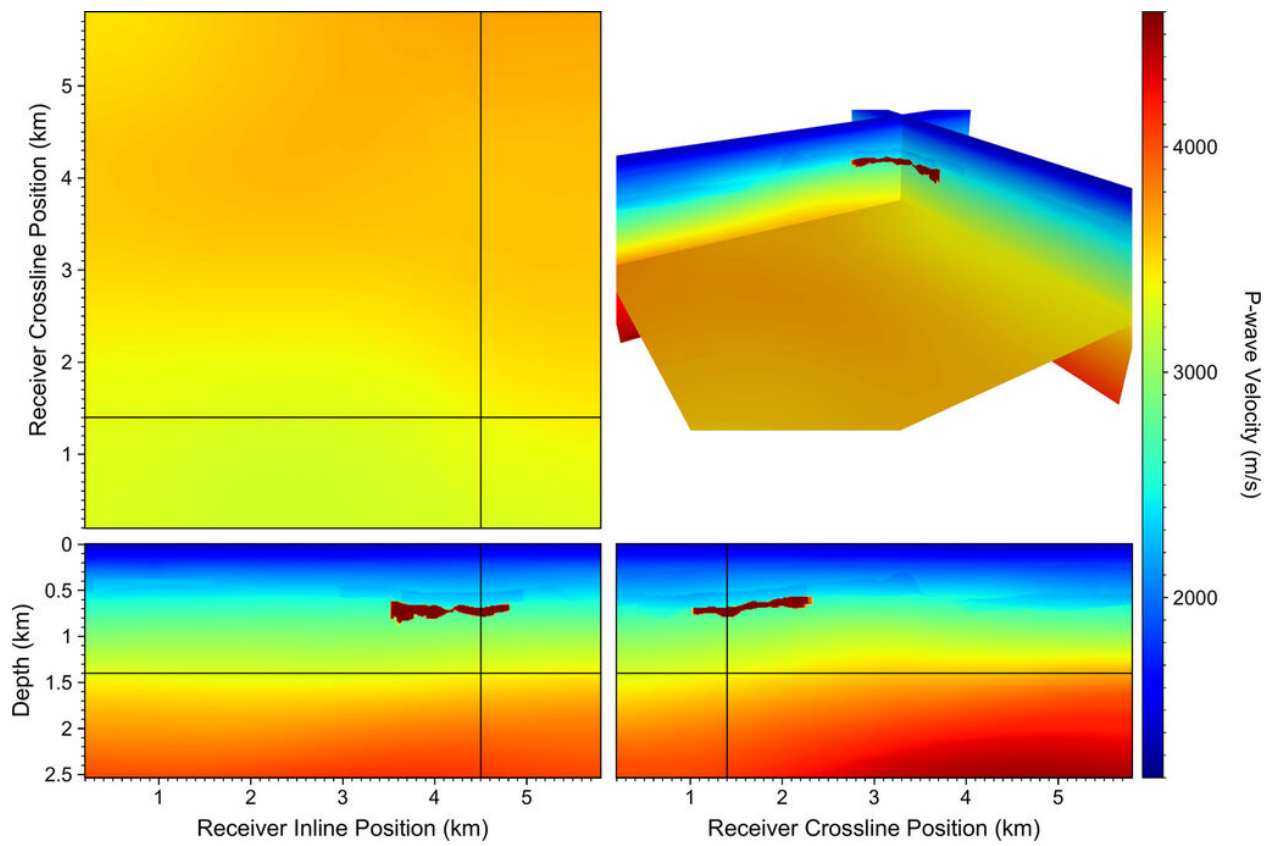


Figure 5: Slices and a 3D view of the initial P-wave velocity model produced by Geokinetics at slicing position 3.

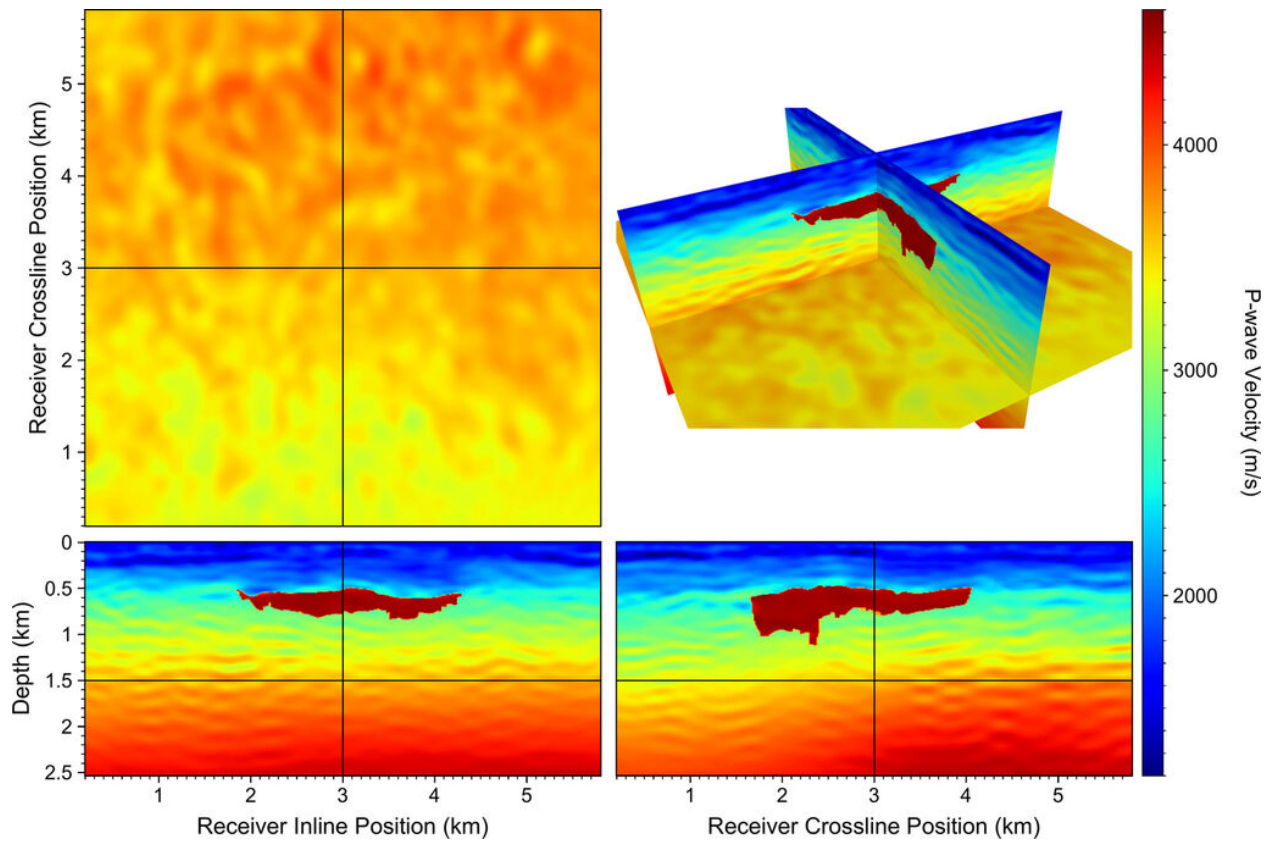


Figure 6: Slices and a 3D view of the updated P-wave velocity model produced using our FWI at slicing position 1 .

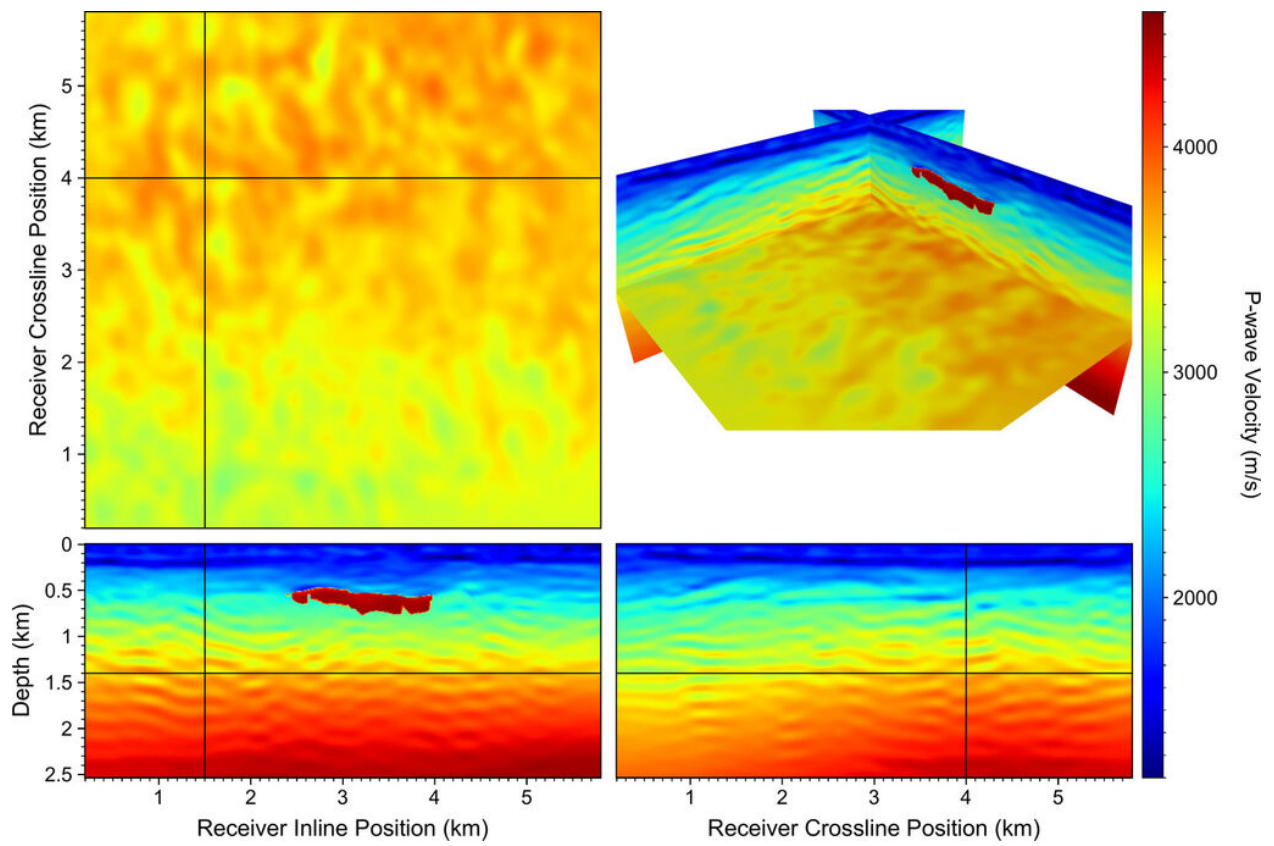


Figure 7: Slices and a 3D view of the updated P-wave velocity model produced using our FWI at slicing position 2.

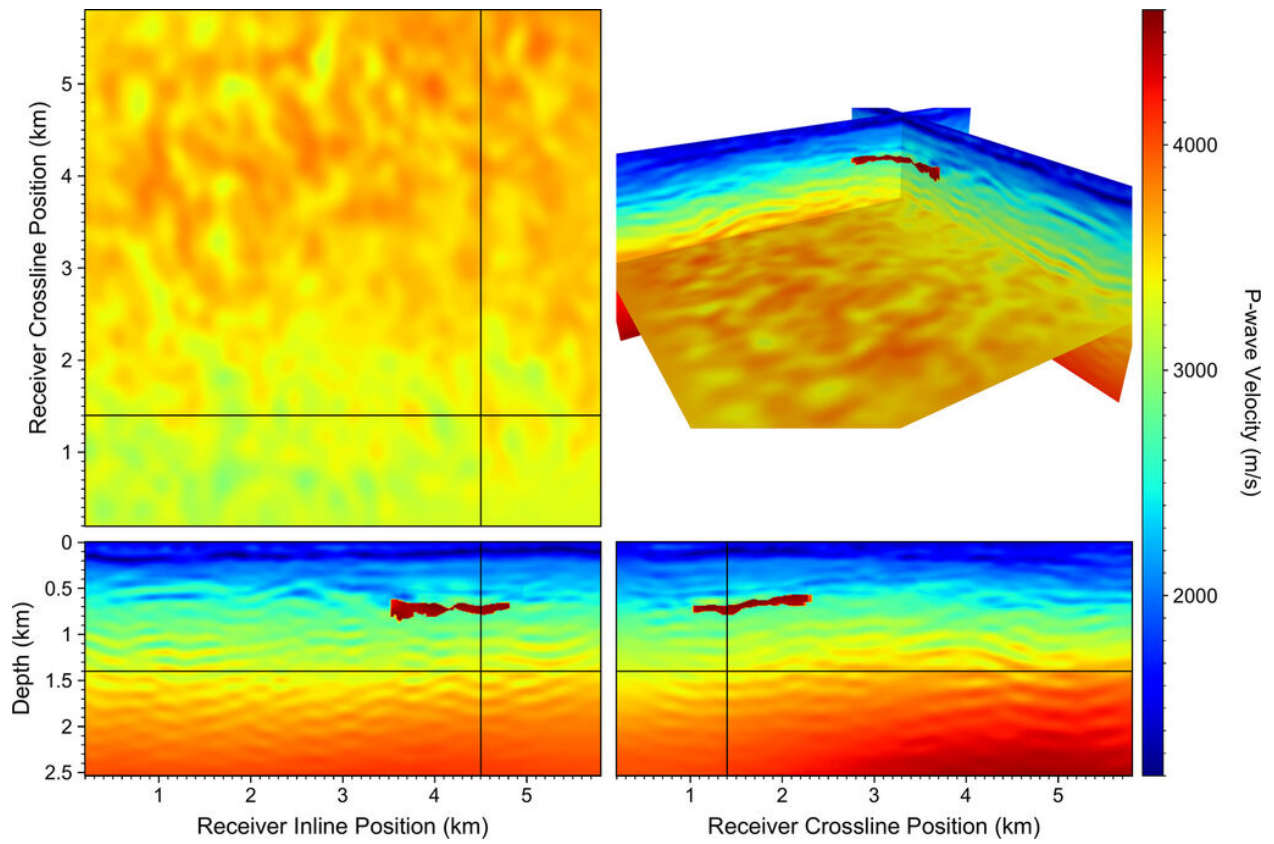


Figure 8: Slices and a 3D view of the updated P-wave velocity model produced using our FWI at slicing position 3.

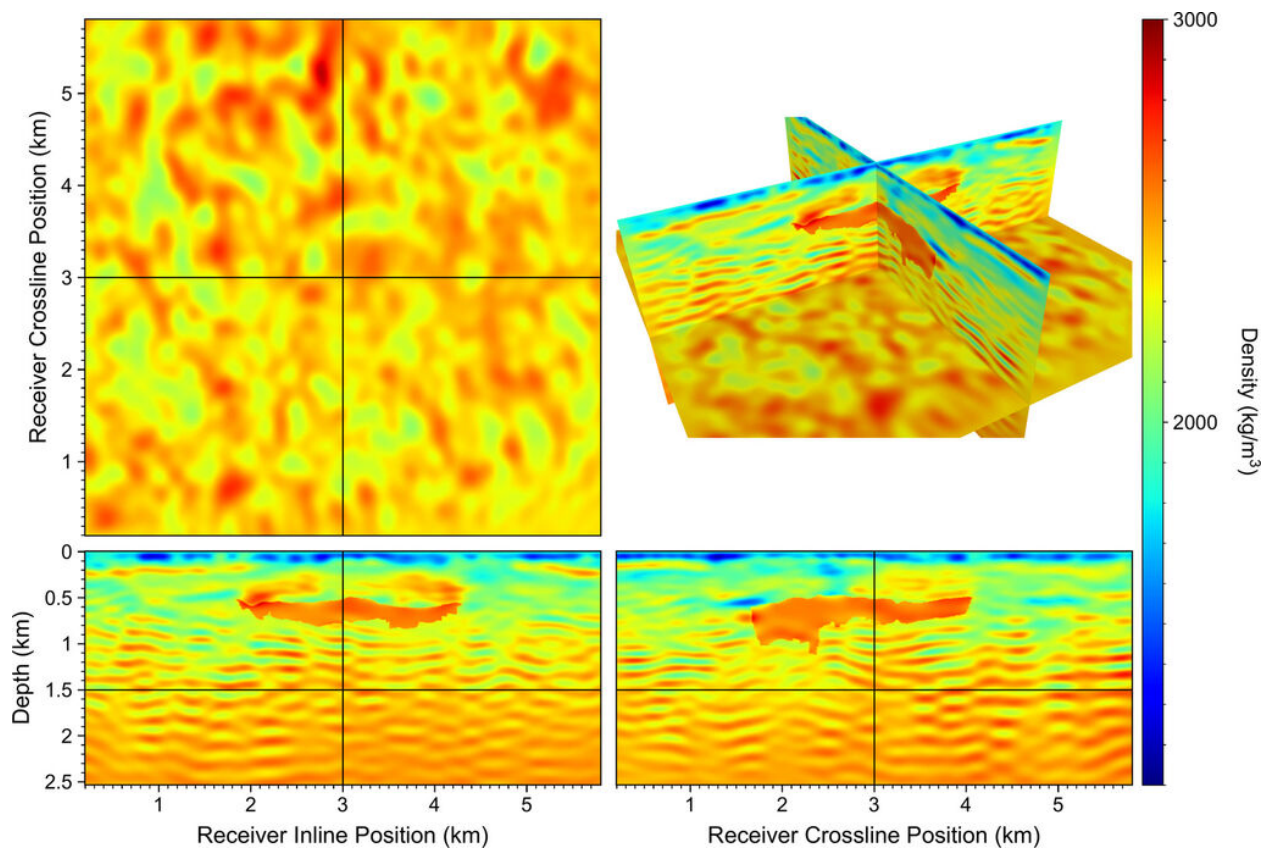


Figure 9: Slices and a 3D view of the updated density model produced using our FWI at slicing position 1.

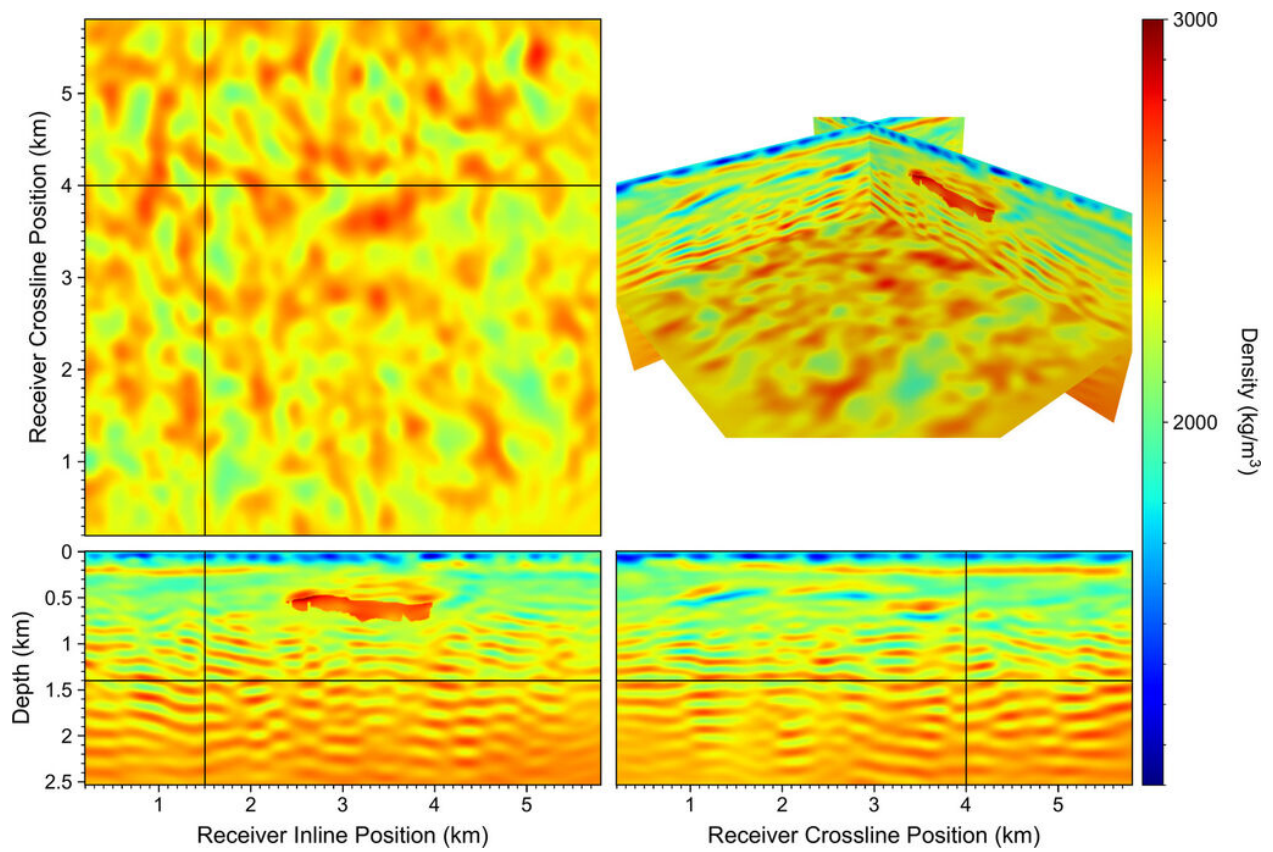


Figure 10: Slices and a 3D view of the updated density model produced using our FWI at slicing position 2.

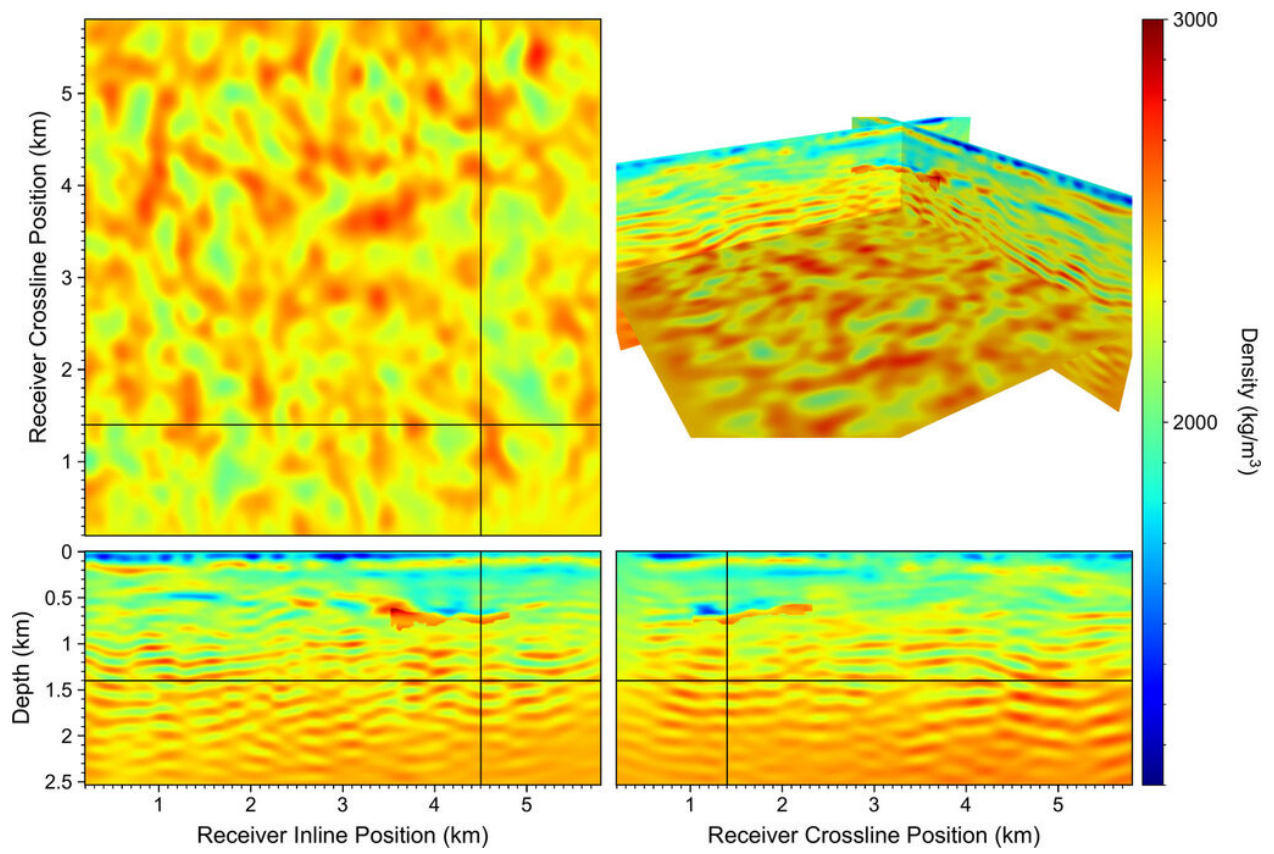


Figure 11: Slices and a 3D view of the updated density model produced using our FWI at slicing position 3.

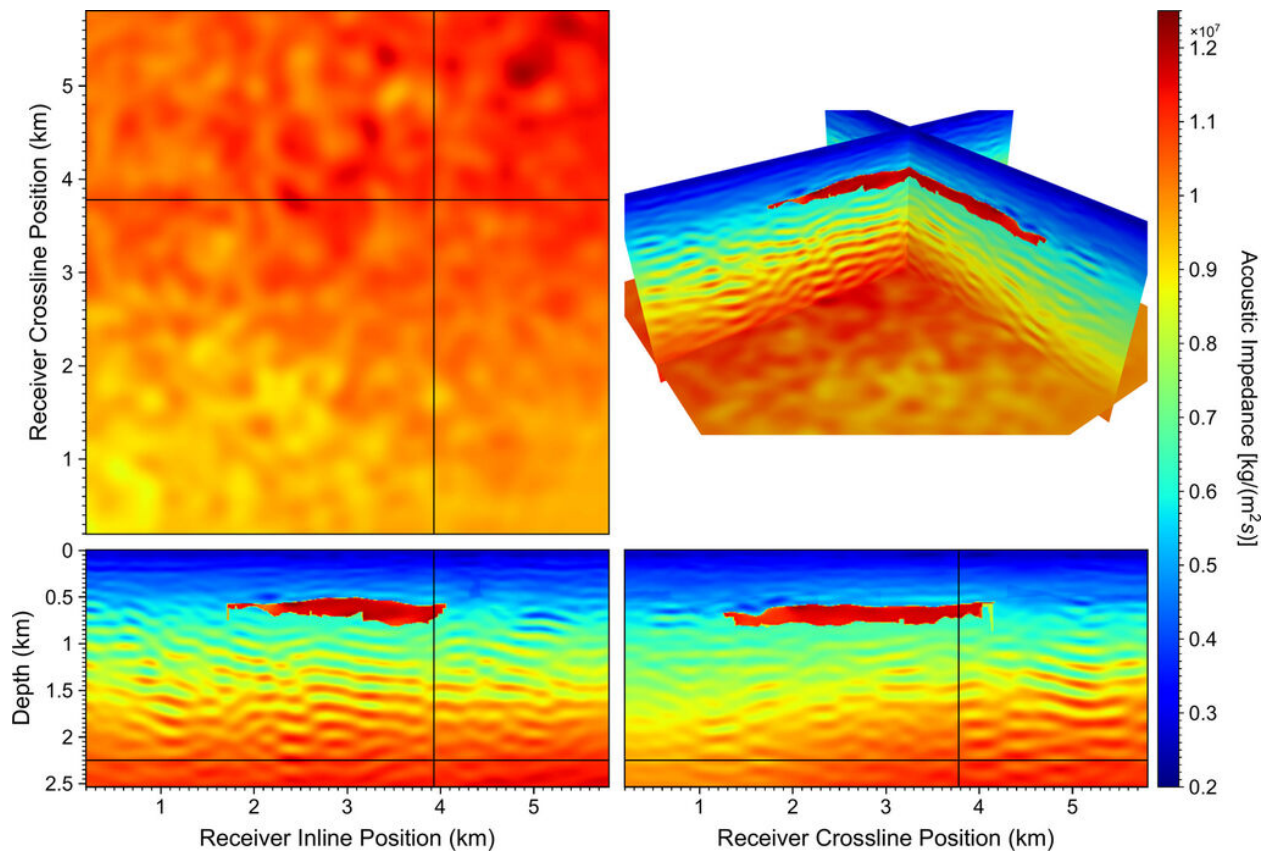


Figure 12: Slices and a 3D view of the updated acoustic impedance model produced using our FWI.

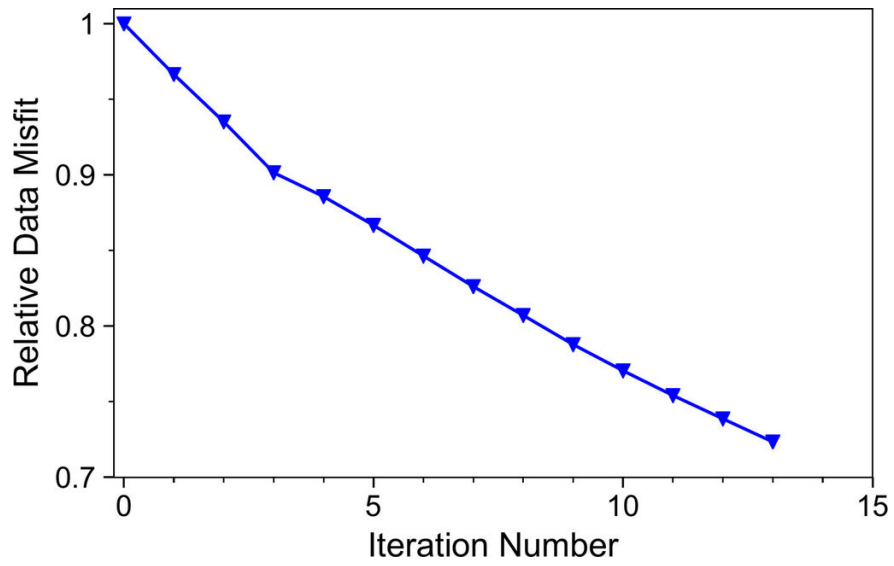
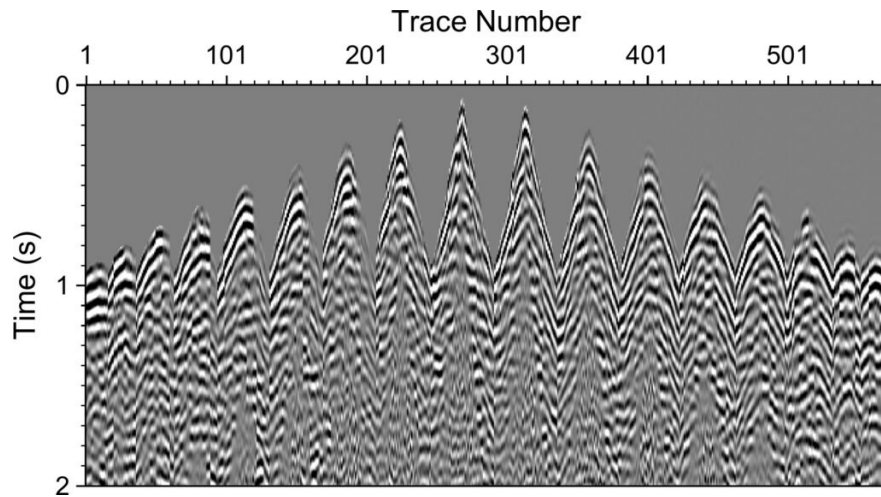
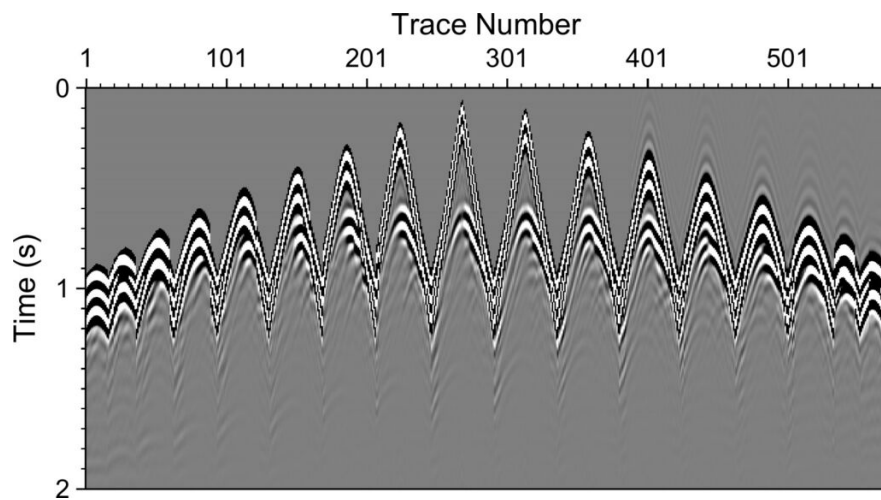


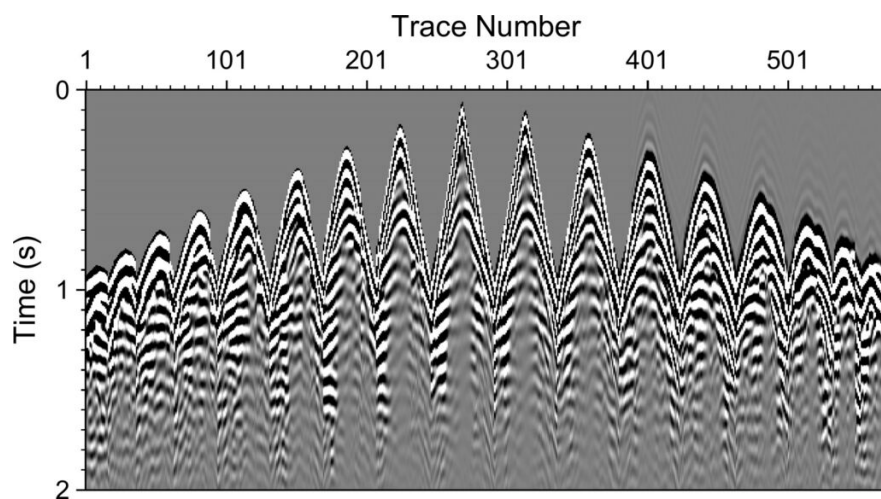
Figure 13: Data misfit convergence over a total of 13 iterations in our FWI.



(a)



(b)



(c)

Figure 14: Panels (a)-(c) show the observed data, the synthetic data in the initial model shown in Figure 3, and the synthetic data in the FWI-updated model shown in Figure 6, respectively.

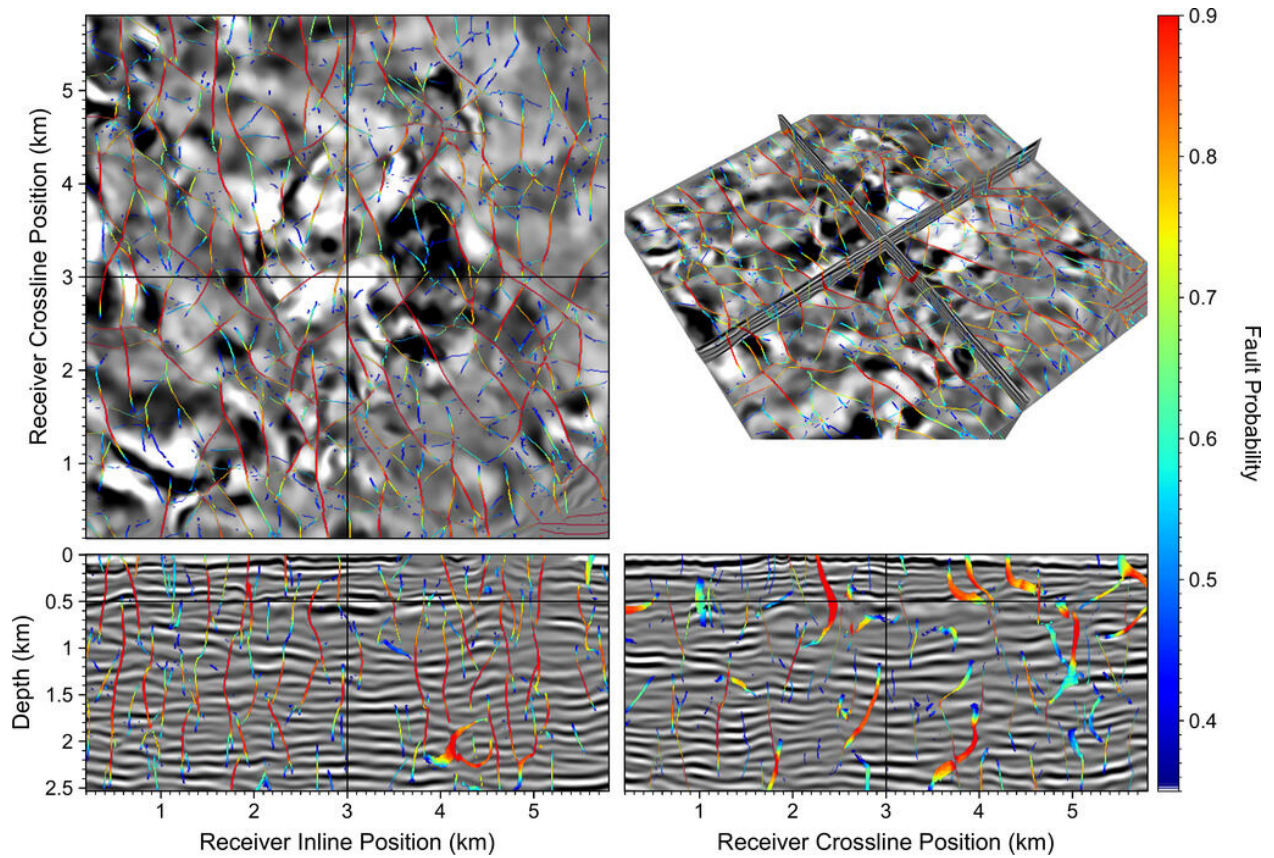


Figure 15: Slices and a 3D view of the structural image of the Soda Lake geothermal field up to 2.5 km in depth produced with our fault-enhancing RTM algorithm, superimposed with the detected faults at slicing position 1.

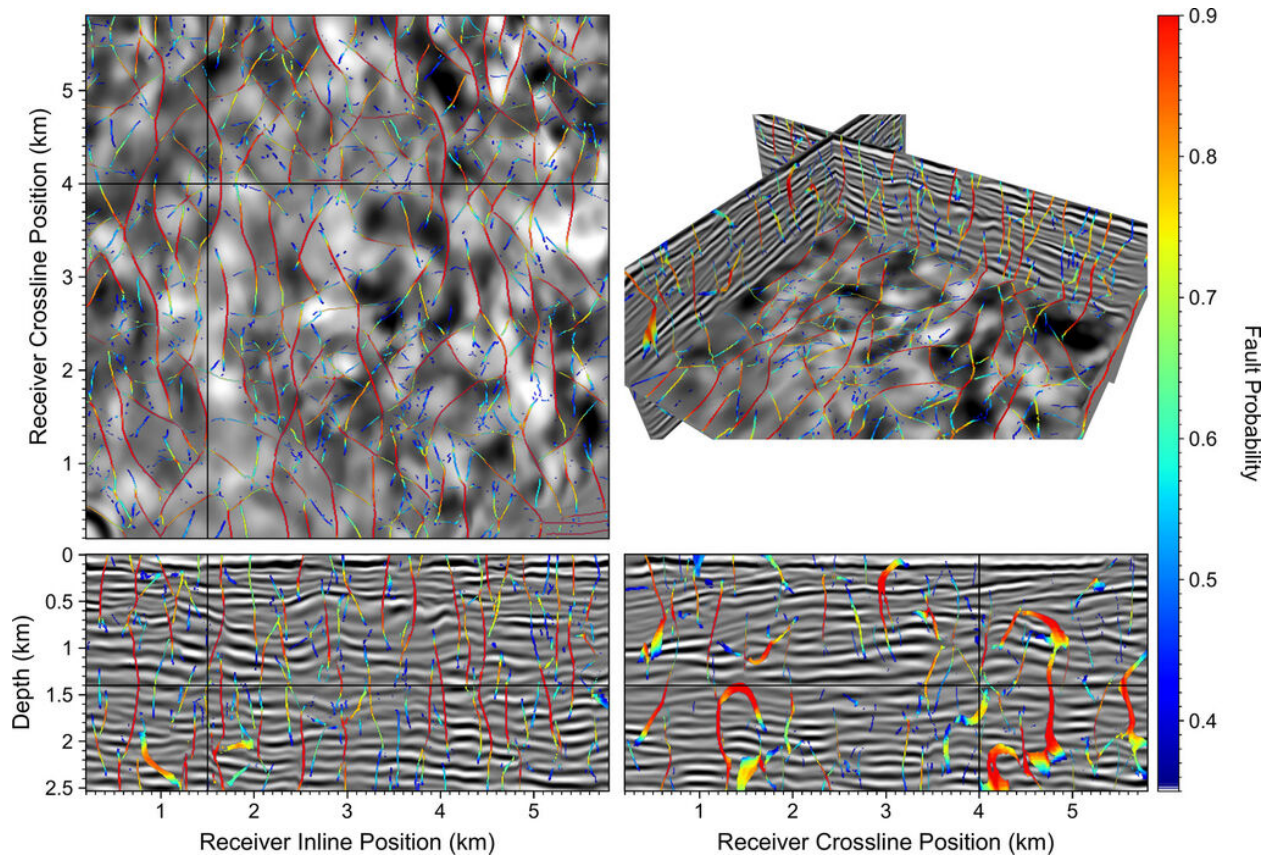


Figure 16: Slices and a 3D view of the structural image of the Soda Lake geothermal field up to 2.5 km in depth produced with our fault-enhancing RTM algorithm, superimposed with the detected faults at slicing position 2.

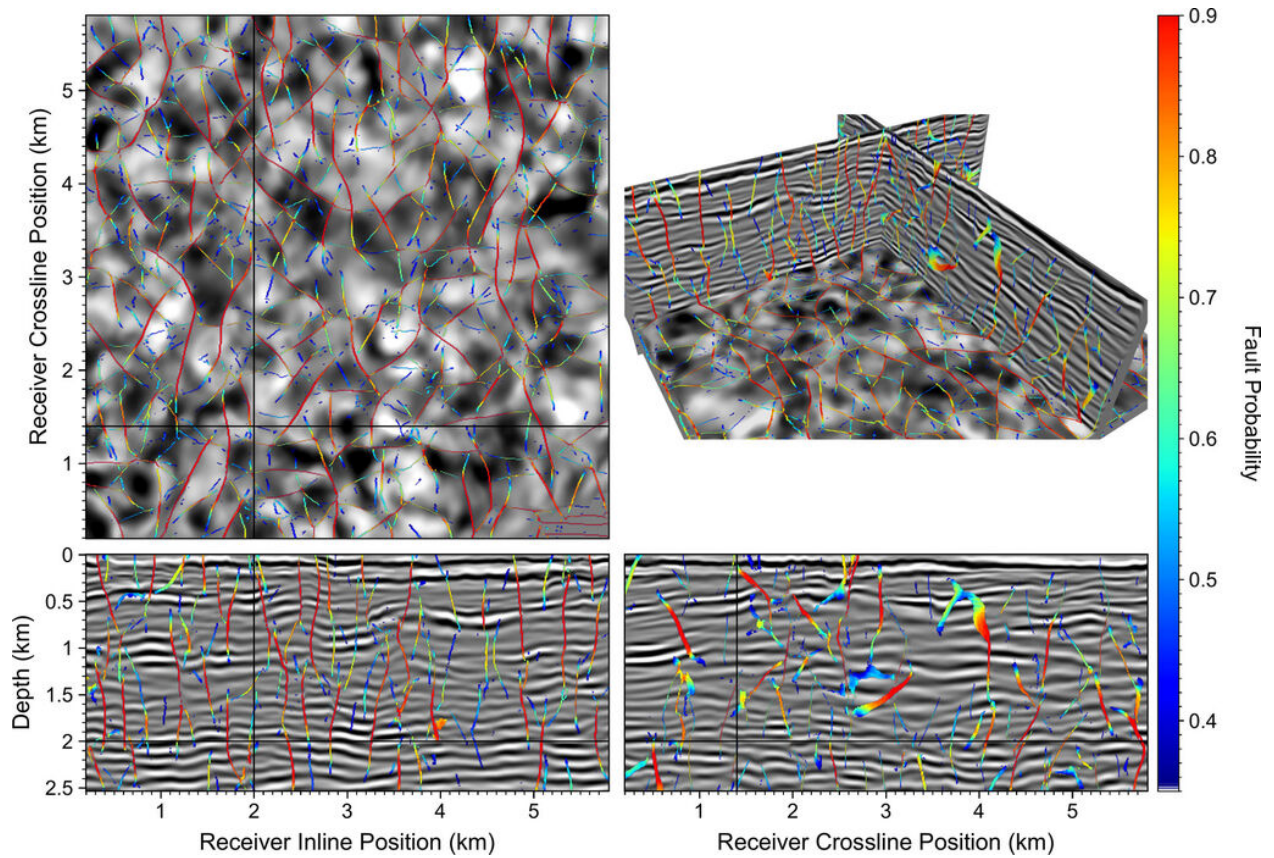
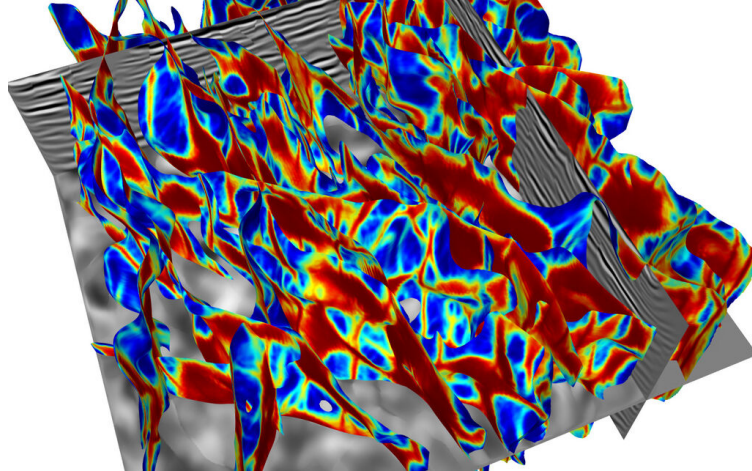
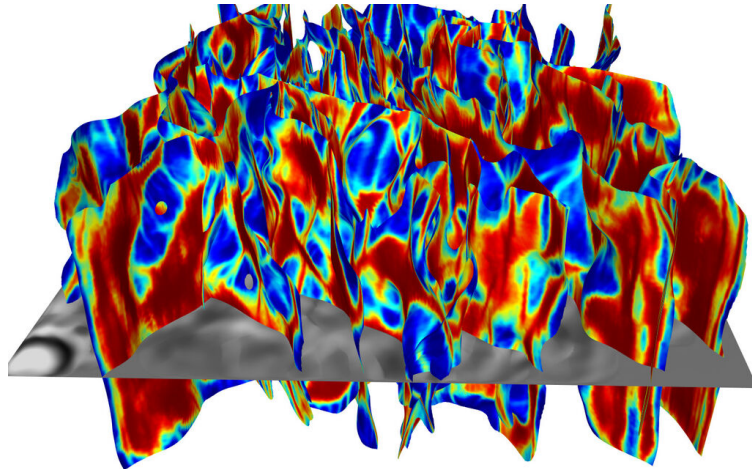


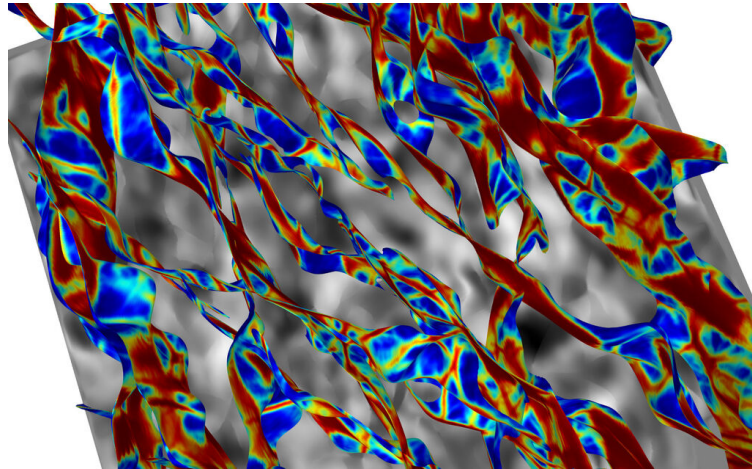
Figure 17: Slices and a 3D view of the structural image of the Soda Lake geothermal field up to 2.5 km in depth produced with our fault-enhancing RTM algorithm, superimposed with the detected faults at slicing position 3.



(a)



(b)



(c)

Figure 18: Panels (a)-(c) show the constructed fault surfaces from the RTM structural image shown in Figure 15 at three different view angles. Colors of the fault surfaces represent the fault probability and are consistent with those in Figures 15-17.

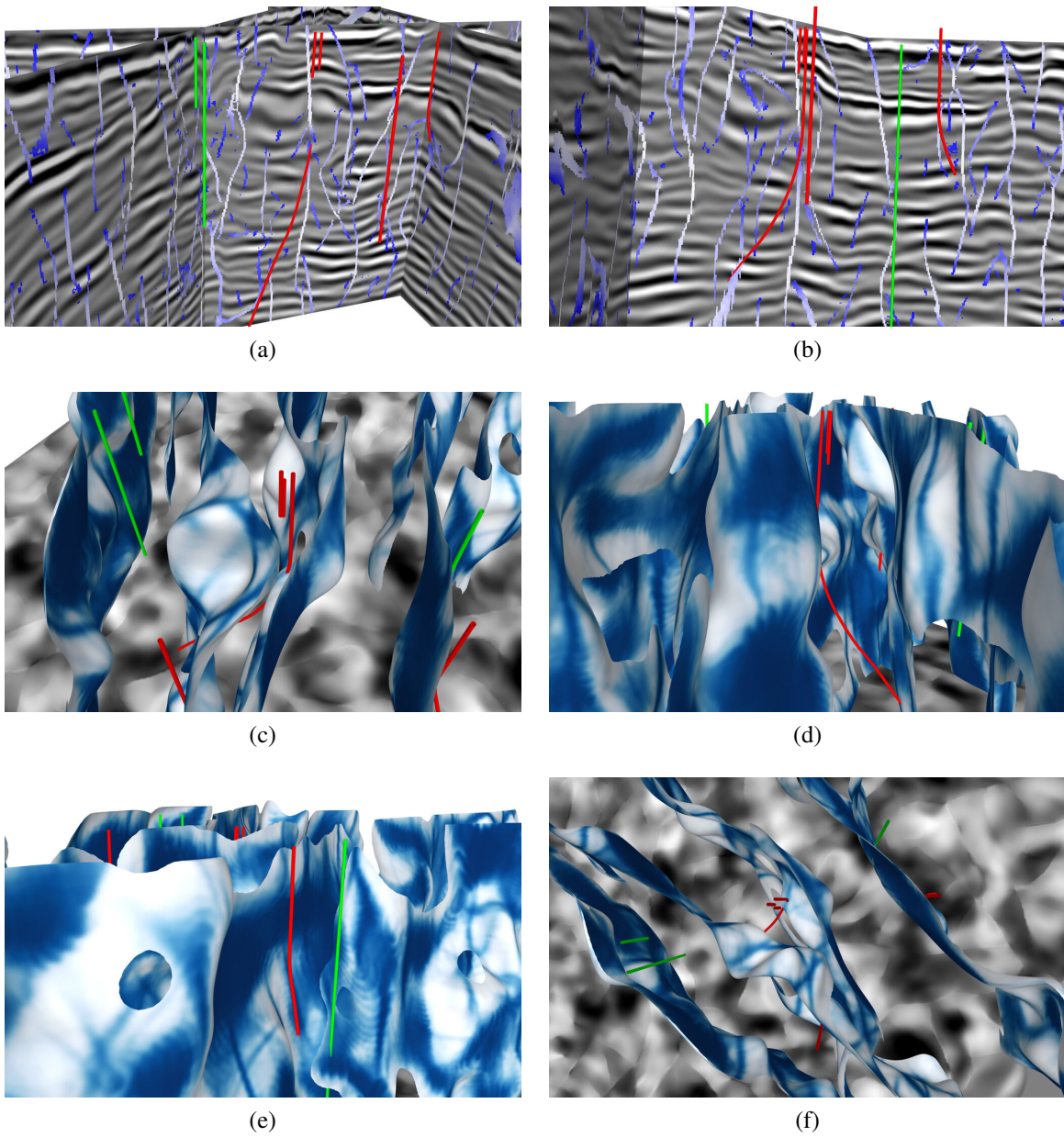


Figure 19: Panels (a)-(b) show the detected faults for the RTM structural image shown in Figure 15 at two different view angles, along with active injection (green) and production (red) wells at the Soda Lake geothermal field. Panels (c)-(f) show the constructed fault surfaces with currently active injection and production wells in this geothermal field.

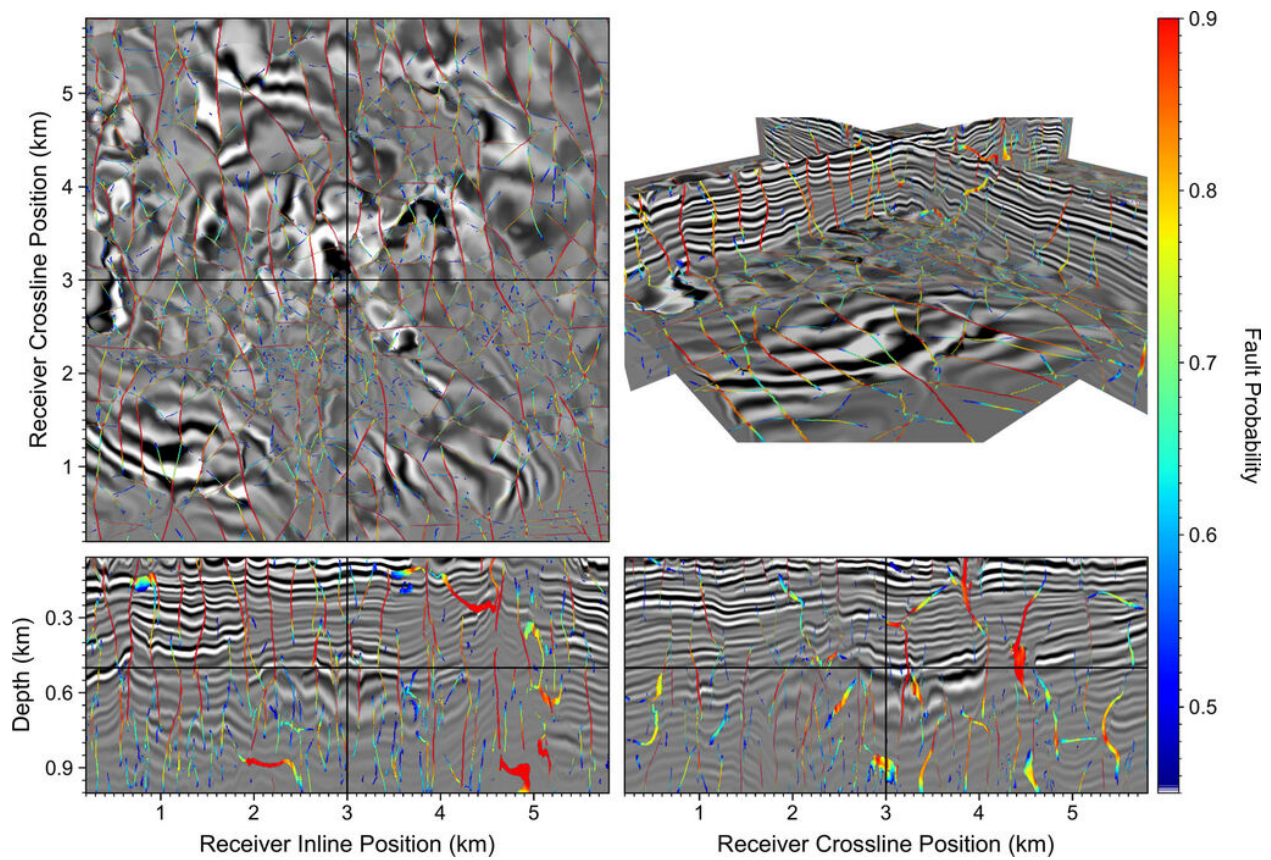


Figure 20: Slices and a 3D view of the structural image up to 1 km in depth produced with our fault-enhancing RTM algorithm, superimposed by the detected faults at slicing position 1.

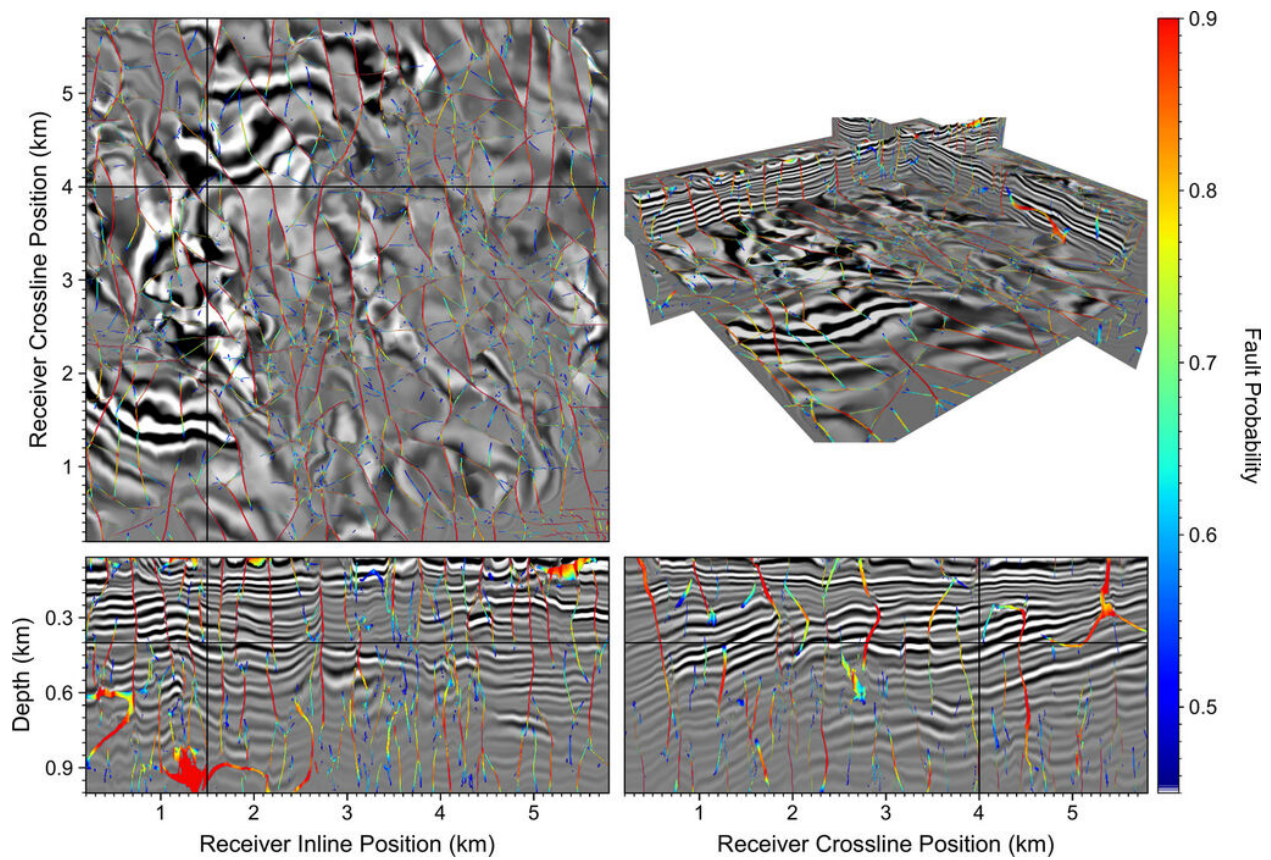


Figure 21: Slices and a 3D view of the structural image up to 1 km in depth produced with our fault-enhancing RTM algorithm, superimposed by the detected faults at slicing position 2.

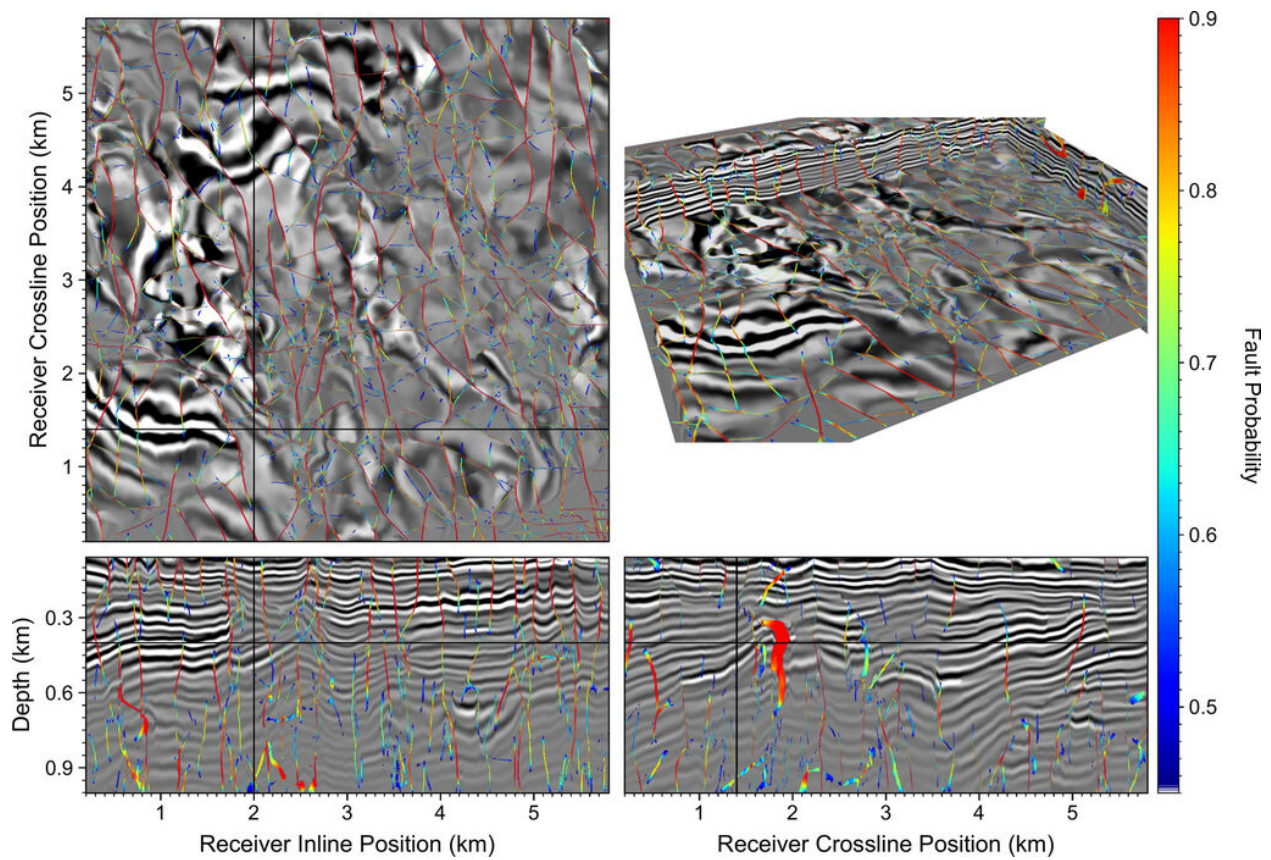
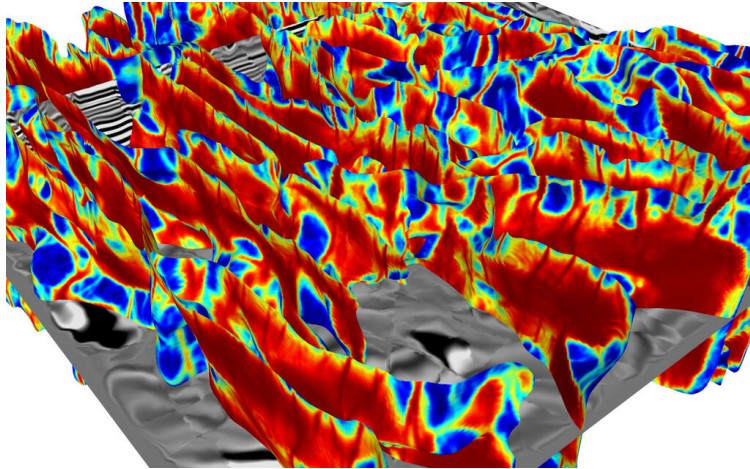
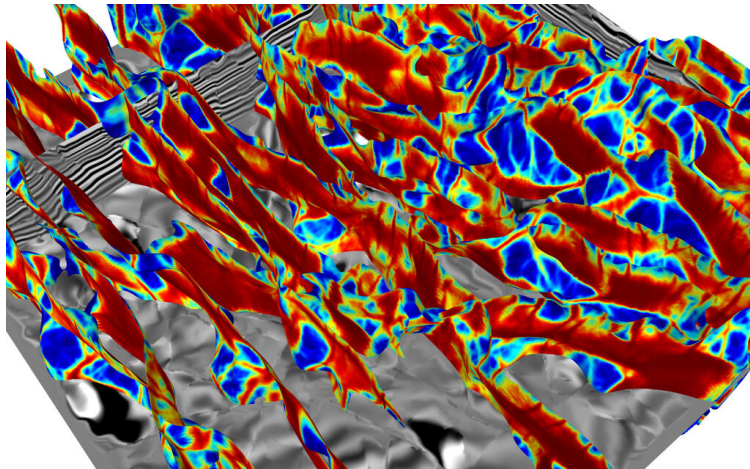


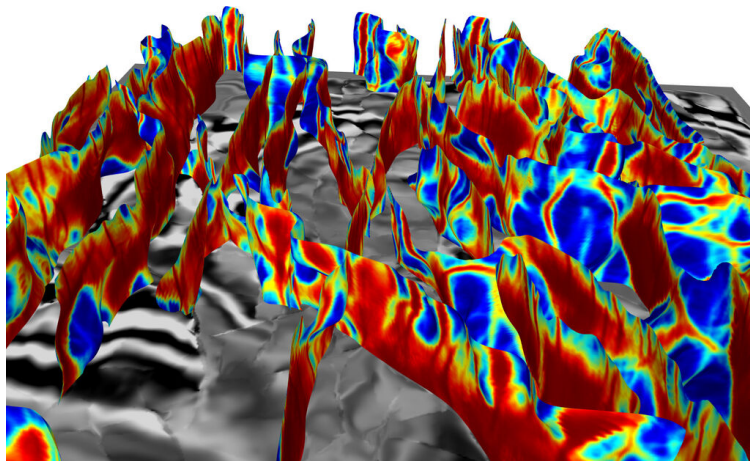
Figure 22: Slices and a 3D view of the structural image up to 1 km in depth produced with our fault-enhancing RTM algorithm, superimposed by the detected faults at slicing position 3.



(a)



(b)



(c)

Figure 23: Panels (a)-(c) show the detected faults from the structural image volume shown in Figure 20 at three different view angles. Colors of the fault surfaces represent fault probability and are consistent with those in Figures 20-22.

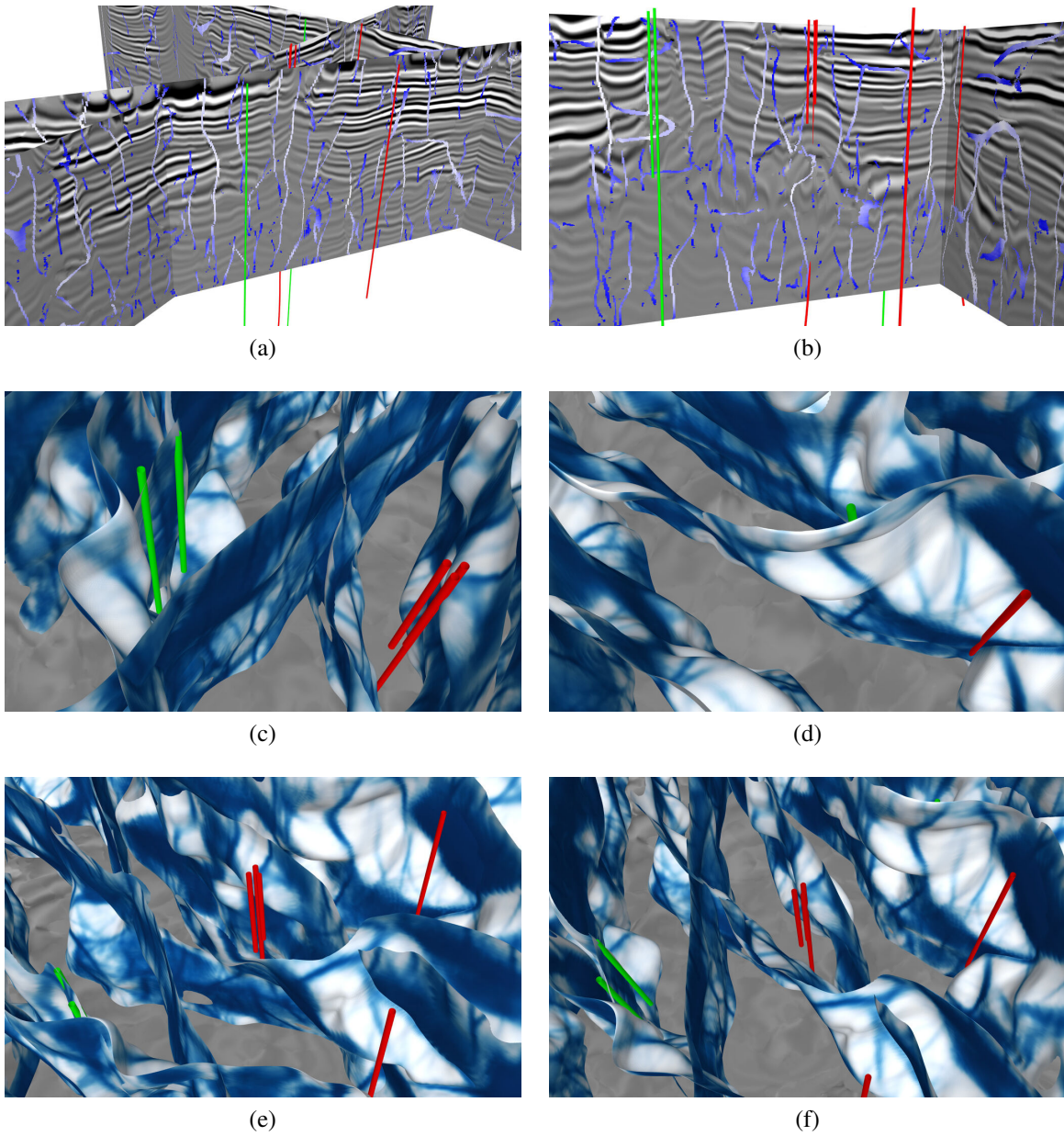


Figure 24: Panels (a)-(b) show the constructed fault surfaces from the structural image shown in Figure 20 at two different view angles, along with active injection (green) and production (red) wells in this area. Panels (c)-(f) depict the constructed fault surfaces with currently active injection and production wells at the Soda Lake geothermal field.